THE MARK II DETECTOR FOR THE SLC*

G. Abrams,[1] C. E. Adolphsen,[2] C. Akerlof,[3] J. P. Alexander,[4],[a] M. Alvarez,[5],[b]
D. Averill,[6] A. R. Baden,[1],[c] J. Ballam,[4] B. C. Barish,[7] T. Barklow,[4]
B. A. Barnett,[8] J. Bartelt,[4] D. Blockus,[6] W. de Boer,[4],[d] G. Bonvicini,[3]
C. Boswell,[8] A. Boyarski,[4] J. Boyer,[1] B. Brabson,[6] K. Braune,[4],[e] A. Breakstone,[9]
J. M. Brom,[6],[f] F. Bulos,[4] P. R. Burchat,[2] D. L. Burke,[4] F. Butler,[1],[g]
F. Calvino,[5],[h] R. J. Cence,[9] J. Chapman,[3] M. Chmeissani,[3] D. Cords,[4]
D. P. Coupal,[4] P. Dauncey,[8] H. C. DeStaebler,[4] D. E. Dorfan,[2] J. M. Dorfan,[4]
P. S. Drell,[1],[a] D. C. Drewer,[8] J. Fay,[1],[i] G. J. Feldman,[4] D. Fernandes,[4]
E. Fernandez,[5],[b] R. C. Field,[4] W. T. Ford,[5] C. Fordham,[4] R. Frey,[3] D. Fujino,[4]
K. K. Gan,[4] C. Gatto,[2] E. Gero,[3] G. Gidal,[1] T. Glanzman,[4] G. Goldhaber,[1]
J. J. Gomez Cadenas,[2],[j] X. Gong,[9] G. Gratta,[2],[k] A. Green,[4],[l] P. Grosse-Wiesmann,[4] J. Haggerty,[1],[m] G. Hanson,[4] R. Harr,[1] B. Harral,[8] F. A. Harris,[9]
C. M. Hawkes,[7] K. Hayes,[4] C. Hearty,[1] D. Herrup,[1],[n] C. A. Heusch,[2]
T. Himel,[4] D. A. Hinshaw,[5] M. Hoenk,[7] S.-O. Holmgren,[1],[o] S. J. Hong,[3]
D. Hutchinson,[4] J. Hylen,[8] W. R. Innes,[4] R. G. Jacobsen,[4] M. Jaffre,[1],[p]
J. A. Jaros,[4] C. K. Jung,[4] I. Juricic,[1],[q] J. A. Kadyk,[1] D. Karlen,[4],[r]
J. Kent,[2] M. King,[2] S. R. Klein,[4] L. Koepke,[2],[e] D. Koetke,[4] A. Koide,[9],[s]
S. Komamiya,[4] W. Koska,[3] L. A. Kowalski,[4] W. Kozanecki,[4] J. F. Kral,[1]
M. Kuhlen,[7] L. Labarga,[2],[t] A. J. Lankford,[4] R. R. Larsen,[4] M. E. Levi,[1]
Z. Li,[7] A. M. Litke,[2] V. Lüth,[4] G. R. Lynch,[1] J. A. McKenna,[7] J. A. J. Matthews,[8]
T. Mattison,[4] B. D. Milliken,[7] K. C. Moffeit,[4] L. Müller,[4],[u] C. T. Munger,[4]
W. N. Murray,[6] J. Nash,[4] M. E. Nelson,[7] D. Nitz,[3] H. Ogren,[6] R. A. Ong,[4],[v]
K. F. O'Shaughnessy,[4],‡ S. I. Parker,[9] C. Peck,[7] J. Perl,[4] M. L. Perl,[4]
F. Perrier,[4],[w] A. Petersen,[4],[x] M. Petradza,[3] R. Pitthan,[4] F. C. Porter,[7]
P. Rankin,[5] J. D. Richman,[1],[y] K. Riles,[4] F. R. Rouse,[1] D. R. Rust,[6]
H. F. W. Sadrozinski,[2] M. W. Schaad,[1] W. B. Schmidke,[1] B. A. Schumm,[1]
A. S. Schwarz,[2],[d] A. Seiden,[2] J. G. Smith,[5] A. Snyder,[6] E. Soderstrom,[7]
D. P. Stoker,[8] R. Stroynowski,[7] M. Swartz,[4] R. E. Taylor,[4] R. Thun,[3] G. H. Trilling,[1] R. Tschirhart,[3],[z] M. Turala,[2],[cc] R. Van Kooten,[4] S. Vejcik,[8]
H. Veltman,[3],[aa] P. Voruganti,[4] S. R. Wagner,[5] S. Watson,[2] P. Weber,[5]
A. Weigend,[4] A. J. Weinstein,[7] A. J. Weir,[7] S. Weisz,[2],[e] S. L. White,[5],[bb]
E. Wicklund,[7] R. C. Wolf,[7] D. R. Wood,[1],[e] M. Woods,[4] G. Wormser,[4],[p]
R. Wright,[4] D. Y. Wu,[7] M. Yurko,[6] C. Zaccardelli,[2] and C. von Zanthier[2]

(1) *Lawrence Berkeley Laboratory and Department of Physics, University of California, Berkeley, California 94720*

(2) *University of California, Santa Cruz, California 95064*

(3) *University of Michigan, Ann Arbor, Michigan 48109*

(4) *Stanford Linear Accelerator Center, Stanford University, ·Stanford, California 94309*

(5) *University of Colorado, Boulder, Colorado 80309*

(6) *Indiana University, Bloomington, Indiana 47405*

(7) *California Institute of Technology, Pasadena, California 91125*

(8) *Johns Hopkins University, Baltimore, Maryland 21218*

(9) *University of Hawaii, Honolulu, Hawaii 96822*

(a) Present address: Cornell University, Ithaca, NY 14853

(b) Present address: Universidad Autónoma de Barcelona, Bellaterra, Spain

(c) Present address: Harvard University, Cambridge, MA 02138

(d) Present address: Max-Planck Institut, München, F. R. Germany

(e) Present address: CERN, CH–1211, Genève 23, Switzerland

(f) Present address: Centre de Recherches Nucleaires, F–67037 Strasbourg, France

(g) Present address: University of Oklahoma, Norman, OK 73019

(h) Present address: Universitat Politecnica de Catalunya, ETSEIB-DEN Barcelona, Spain

(i) Present address: IPN Lyon, F–69622 Villeurbanne, France

(j) Permanent address: IFIC, Valencia, Spain

(k) Permanent address: Università di Roma I, Roma, Italy

(l) Present address: O'Conner and Associates, Chicago, IL 60604

(m) Present address: Brookhaven National Laboratory, Upton, NY 11973

(n) Present address: Fermilab, Batavia, IL 60510

(o) Present address: University of Stockholm, Stockholm, Sweden

(p) Present address: Laboratoire de l'Accélérateur Linéaire, F–91405 Orsay, France

(q) Present address: Columbia University, New York, NY 10027

(r) Present address: Carleton University, Ottawa, Ontario, Canada, K1S 5B6

(s) Present address: Vista Research Inc., P. O. Box 998, Mountain View, CA 94042

(t) Permanent address: Universidad Autónoma de Madrid, Madrid, Spain

(u) Present address: Lab. für Hochenergie Physik Bern, CH–3012 Bern, Switzerland

(v) Present address: University of Chicago, Chicago, IL 60637

(w) Present address: CEN Saclay, Gif-sur-Yvette, France

(x) Present address: SCS, Hamburg, F. R. Germany

(y) Present address: University of California, Santa Barbara, CA 93106

(z) Present address: Princeton University, Physics Department, Princeton, NJ 08544

(aa) Present address: University of California, Berkeley, CA 94720

(bb) Present address: University of Tennessee, Knoxville, TN 37996

(cc) Present address: Institute of Nuclear Physics, Kraków, Poland

‡ Editor

ABSTRACT

The Mark II detector has been upgraded in preparation for its role as the first detector to take data at the Stanford Linear Collider. The new detector components include the central drift chamber, the time-of-flight system, the coil, the endcap electromagnetic calorimeters and the beam energy and luminosity measuring devices. There have also been improvements in detector hermeticity. All of the major components were installed for a test run at the PEP storage ring ($\sqrt{s} = 29$ GeV) in 1985. This paper describes the upgraded detector, including its trigger and data acquisition systems, and gives performance figures for its components. Future improvements are also discussed.

TABLE OF CONTENTS

1. INTRODUCTION

The Mark II detector is the first detector to take data at the Stanford Linear Collider (SLC) [1]. The SLC provides electron-positron colliding beams with a center-of-mass energy around the Z^0 resonance (approximately 92 GeV). The detector is an upgraded version of the device previously used successfully at the PEP and SPEAR storage rings. Newly constructed components include the central drift chamber, the time-of-flight system, the coil, the endcap electromagnetic calorimeters and the luminosity monitors [2]. There have also been improvements in detector hermeticity. In addition, spectrometers for making precise measurements of both electron and positron energies on a pulse-by-pulse basis have been designed and implemented. Finally, several further additions to the detector (new vertex detectors, increased muon coverage and online processors) are being constructed and tested but are not currently installed. They will be briefly discussed at the end of the paper.

A cut-away view of the detector can be seen in fig. 1. Emerging from the interaction point, a particle emitted perpendicular to the beam would traverse the beampipe, the central drift chamber, a time-of-flight counter, the coil of the solenoid magnet, the liquid argon calorimeter and finally the muon detection system. The following sections describe these components as well as the endcap calorimeters and small-angle monitors. When available, performance figures from a test run at PEP (29 GeV center-of-mass energy) are quoted. For systems not installed for the test run at PEP, data from test beam studies or Monte Carlo simulations are presented.

2. CENTRAL DRIFT CHAMBER

A new central drift chamber was built to improve the momentum resolution, the two-track separation and the pattern recognition. Some charged particle identification capability through dE/dx measurements is also provided.

2.1 Drift Chamber Design

The drift chamber design is based on a six sense-wire cell, a shortened version of the jet-chamber configuration [3]. The cells are arranged in 12 concentric cylindrical layers, alternating between wires parallel to the cylinder axis (axial layers) or inclined at approximately $\pm 3.8°$ to the axis to provide stereo information. The inner radius of the drift chamber is 19.2 cm, the outer radius is 151.9 cm and the active length is 2.30 m. The design parameters are given in table 1.

The detailed cell design is shown in fig. 2. The sense wires (30-μm-diameter gold-plated tungsten) are staggered ± 380 μm from the cell axis to provide local left-right ambiguity resolution. The electric field is controlled primarily by the voltage on a row of 19 field wires at each edge of the cell. There are also guard and potential wires interspersed with the sense wires which help to adjust the electric field and the gains on the sense wires.

The wires are strung between 5.1-cm-thick aluminum endplates which are held apart by a 2-mm-thick beryllium inner cylinder and a 1.27-cm-thick aluminum outer shell. In addition there are eight 2.5-cm by 5.1-cm aluminum ribs attached to the outer shell which provide structural support. The aluminum shell and beryllium cylinder are lined with skins of copper-clad Kapton; a voltage is applied to these skins to maintain a uniform electric field in the innermost and outermost layers.

The wires in one plane in a cell are located in machined notches in a Delrin feedthrough which is pinned to accurately machined holes in the endplate. The average uncertainty in wire location is 35 μm and is primarily due to errors in machining and placement of the feedthroughs and endplates. A more detailed description of the chamber design can be found in ref. 4.

2.2 Electronics

The drift chamber signals are amplified in two stages and then digitized. Both a time digitization and a pulse shape digitization (allowing the dE/dx measurement) are made. Figure 3 is a schematic drawing of the drift chamber electronics.

The preamplifier (first stage) boards are mounted directly on the feedthroughs at the chamber face, inside an aluminum RF shield. The circuitry is based on the Plessey SL560C chip. The second stage of amplification is performed by the 24-channel postamplifiers located in crates mounted on the magnet iron. In addition, these boards shape and split the signal. The timing half of the postamplifier has a gain of 70 and discriminates the pulses using a LeCroy MVL407 comparator. The threshold set for the comparator corresponds to 80 μV at the preamp input. This is equivalent to 4% of the mean pulse height due to a minimum ionizing particle. The gain setting for the pulse height measurement can be varied. More details on the preamplifiers and postamplifiers can be found in ref. 5.

At this point the two sets of signals (timing and pulse shape) are brought out approximately 30 m to the electronics house. The drift times are digitized by 96-channel LeCroy 1879 TDCs located in four FASTBUS crates. These modules have multi-hit capability and a time bin width of 2 ns. The drift chamber pulse shapes are digitized by SLAC-designed [6] FASTBUS boards. These boards are 16-channel 100-MHz Flash-ADCs with 6-bit resolution based on the TRW 1029J7C chip. (For the test run at PEP, only one-third of the drift chamber was instrumented with FADCs.)

The readout of both the TDCs and FADCs is controlled by SLAC Scanner Processors (SSPs) [7], which are programmable FASTBUS modules. One SSP is used in each FASTBUS crate to preprocess (e.g., perform zero suppression and pedestal corrections) and format the data. The crate SSPs are read out via cable segments by system SSPs, which buffer the data and interface with the experiment host computer, a VAX 8600. Programs on the host computer correlate the TDC and FADC hits on each wire. The timing and pulse height channels are calibrated

separately. For both, the calibration pulse is injected at the input to the pream-plifier. The timing calibration measures the time propagation differences for each channel. The pulse height calibration is used to determine a pedestal, gain and quadratic correction for each channel.

2.3 Operation

A graded high voltage is supplied to the field wires of each cell through a resistor-divider chain. The voltage on a field wire in the center of a cell is typically -4.5 kV, the potential wire and guard wire voltages are typically -1.5 kV and -200 V, respectively, and the sense wires are grounded. The copper skins lining the inner and outer cylinders are typically set at -2.5 kV. The drift chamber high voltages and currents are controlled and monitored using an IBM PC.

The chamber gas is a mixture of 89% Ar, 10% CO_2 and 1% CH_4 (HRS gas) and is at a pressure slightly above 1 atmosphere. The above voltages result in a gas gain of 2×10^4 with an electric drift field of 900 V/cm and the typical drift velocity is 52 μm/ns. For most of the test run at PEP the magnetic field was 4.5 kG, giving a Lorentz angle of 17.8°.

2.4 Performance

2.4.1 Tracking efficiency

The drift chamber tracking program was implemented using hits found by the TDCs. It utilizes the multi-sense-wire feature of the cells and forms track segments within cells. These segments are later matched to form tracks through the chamber [8]. The track-finding routine efficiency has been measured at PEP and estimated for SLC from Monte Carlo programs. For low multiplicity events at PEP with tracks that go through all sublayers, the efficiency was measured to be approximately 99%. It is estimated to drop to 96% for high multiplicity hadronic events of the type expected at SLC energies. Figure 4 shows the efficiency as a function of cos θ for these two classes of events.

10

2.4.2 Position and momentum resolution

The position resolution in the chamber is primarily limited by diffusion in the gas. Calculations show that this effect contributes an error of ≈ 150 μm for the longest drift distances. Other errors are ≈ 50 μm from the time measurement error in the electronics and ≈ 35 μm from wire placement. When a single drift velocity was used for all cells and layers to convert the drift times to positions, the achieved resolution averaged over the cell width was 185 μm. Fitting velocities for each of three drift distance regions in a cell and for different groups of wire layers improved the resolution to ≈ 170 μm.

The information from the FADCs can be included in the timing measurement by using the deposited charge to make a "time-slewing" correction. This correction compensates for the change in measured time as a function of pulse height and improves the resolution by a small amount. Figure 5 shows the resolution versus drift distance with and without the time-slewing correction. However, the major tracking improvement provided by the FADCs is a better double hit separation. Scanning algorithms that use the pulse shape have an efficiency of 80% for separating hits 3.8 mm apart compared to 6.4 mm if only the TDCs are used (see fig. 6).

From Bhabha scattering events in the PEP data taken with a 4.5 kG field, a momentum resolution of $\sigma(p)/p^2 = 0.46\%$ $(GeV/c)^{-1}$ was measured in the central drift chamber for single tracks with $|\cos\theta| < 0.64$. The resolution is $\sigma(p)/p^2 = 0.31\%$ $(GeV/c)^{-1}$ if the tracks are constrained to originate from a single point (see fig. 7). The multiple scattering contribution to the resolution from the drift chamber itself is 1.4%. Beam diagnostic devices and other material inside the drift chamber radius also contribute to the vertex constrained resolution through multiple scattering.

2.4.3 Particle identification

The main purpose of the FADC system is to provide some degree of particle identification, particularly for separating electrons from pions. The charge deposited by a particle traversing the drift chamber is proportional to its energy loss (dE/dx). The value of dE/dx coupled with the measured momentum allows a rough determination of the particle mass. For a track travelling the full radial extent of the central drift chamber, the 72 possible charge measurements would provide an expected dE/dx resolution for minimum-ionizing particles of 6.9% [9].

The FADC pulse shapes are processed to provide the time and integrated charge for each hit. The "difference of samples" algorithm [10] that is currently used scans the pulse and looks for sharp changes in its shape. The time is determined by a weighted average over the bins where there is a change, and the charge is calculated by summing the counts between the start and end of the pulse as identified by the algorithm.

The charge collected depends on the path length, the angle that the track makes with the wire, the drift distance, and whether the staggered sense wire is on the near or far side of the wire plane from the track. There are also variations in the gas gain due to pressure and temperature, differences in gain in each of the 72 sublayers of the drift chamber, and variations from channel-to-channel due to the electronics. After correcting each measured charge for these effects, a (75%) truncated mean of the samples is calculated to arrive at a dE/dx value for the track. The corrected values are shown as a function of momentum for particles at PEP in fig. 8. The different particle types were identified using other detector components or event topologies.

From a sample of Bhabha scattering events from PEP data, a dE/dx resolution of 7.2% was obtained. Figure 9 shows the resulting separation between electrons and pions for tracks in a momentum range of 0.25 GeV/c to 0.60 GeV/c. The electrons were identified using the barrel electromagnetic calorimeter and pions were defined as tracks that were not identified as electrons, kaons or protons.

12

The peaks were obtained from different event samples within the same data runs. Electron-hadron separation for all momenta is discussed in the next chapter.

3. TIME-OF-FLIGHT SYSTEM

The time-of-flight (TOF) system is used to provide charged particle identification including the detection of cosmic rays. The time is measured by detecting signals generated in scintillator slabs located between the central drift chamber and the magnet coil.

3.1 Physical Description

The TOF system consists of 48 counters forming a barrel of inner radius 152.4 cm that is outside and coaxial with the central drift chamber. Each counter is 300 cm long and has a trapezoidal cross section with a smaller width of 19.8 cm. The counters are 4.5 cm thick except for two counters bordering $\phi = 0°$ and two counters bordering $\phi = 180°$ which are 3.8 cm thick. The addition of eight structural ribs along the drift chamber body (which are equally spaced in ϕ starting at $\phi = 0°$) required cutting 1.6 cm from the width of the 16 adjacent counters. The counters are cast from a plastic scintillator based on cross-linked polystyrene (SCSN–38 [11]) which was chosen for its high resistance to crazing due to mechanical stress. The mounting system was designed to provide stress-free support. Both ends of the counters are coupled to light guides made from UV-light-transmitting acrylic. These guides narrow from the width of the counters (an average of 20 cm) to 5.3 cm over a length of 43 cm and then extend 84 cm further to bring the light outside the flux return iron. An Amperex XP2222 12-stage photomultiplier tube is attached to the end of each light guide, with optical coupling provided by a soft Sylguard "cookie" [12]. The phototubes are shielded from stray magnetic fields by concentric cylinders of mu-metal and soft iron. CAMAC-controlled LeCroy 4032A high voltage supplies power the voltage dividers in the phototube base. These voltage dividers have been designed to minimize phototube transit time jitter.

3.2   Electronics

The electronics of the data acquisition system are those used by the pre-upgrade Mark II at PEP [13]. Each phototube channel consists of two independently discriminated Time-to-Amplitude Converters (TACs) and a pulse height integrator. The analog times and pulse integrals are collected and digitized by a 12-bit ADC incorporated in a 16-bit microprocessor (BADC) [14]. The BADC then performs pedestal subtractions, linear gain corrections, and threshold cuts to the raw digitized values. The timing acceptance window is 60 ns which is large enough for the possible observation of slow particles, but which also allows for rejection of cosmic rays.

3.3   Calibration Systems

There are two independent calibration systems. The calibration of the electronics is carried out using a variable amplitude pulser and delay cables of known length. Calibration constants are computed using a second order fit of channel response to input pulses. These constants provide an accuracy of $\sigma = 60$ ps over a 35-ns interval for the TACs and $\sigma = 70$ pC over a 1700 pC range for the pulse height integrators.

The laser calibration system, illustrated in fig. 10, monitors the response of the counters and associated electronics to short light pulses which simulate the effect of charged particles passing through the scintillator. A pulsed nitrogen laser illuminates optical fibers attached to each counter 90 cm from each end. A CAMAC-controlled mirror allows for the illumination of one fiber at a time in the system, and a set of neutral density filters allows for variation of input light intensity. The timing reference is provided by a photodiode exposed to the laser light; the photodiode also measures the intensity of each pulse. The system provides enough redundant information to monitor the gains of the phototubes, the propagation delays through the scintillator, light guides, cables and electronics and the attenuation length of the scintillator. It has been observed that the phototube current

14

saturates at high light levels in the scintillator. A correction for this saturation with the same functional form for each phototube is determined using the laser calibration system.

3.4 Data Analysis

The measured times from each phototube are corrected for the time that the light takes to propagate through the scintillator and for channel-to-channel propagation delays through the phototube. The saturation correction is applied, then a time walk correction [15] proportional to the inverse square root of the corrected pulse integral is also applied. The time walk constant is determined for each phototube using the data from the test run at PEP. A final time of flight t is obtained by taking the weighted average of the times from both phototubes.

Particle identification is determined from the velocity $\beta = L/(ct)$, where the path length L from the interaction point is determined from the central drift chamber information and t is the time of flight. The squared mass of the particle is then given by $m^2 = p^2 \left[1/\beta^2 - 1 \right]$, where p is the particle momentum as measured by the drift chamber.

3.5 Performance

Figure 11 shows the difference between the time measured by the TOF system and the expected time of arrival of electrons from the Bhabha scattering process $e^+e^- \rightarrow e^+e^-$ measured during the PEP test run. The achieved single counter resolution varied from 180 to 250 ps and averaged over all counters and all data runs was 221 ps. This gives the $\pi/K/p$ separation shown in fig. 12. The measured TOF and dE/dx resolutions are combined to give the electron-hadron separation seen in fig. 13. The two systems together also give at least a 2σ π/K separation up to momenta of 10 GeV/c and K/p separation up to 2.0 GeV/c in momentum. However, it should be pointed out that the resolutions in high-multiplicity events will be slightly worse, implying poorer separation in those classes of events.

The reassembled TOF system at the SLC experimental hall is monitored by the same laser calibration system which has shown that the constants leading to the resolution achieved at PEP are still valid. Data from cosmic rays at the SLC provide further evidence that the resolution remains at the previous level.

4. MARK II SOLENOID

The Mark II solenoid is a conventional cylindrical coil producing a magnetic field of up to 5.0 kG in the center of the detector. Its thickness is 1.3 radiation lengths. The coil consists of twelve aluminum conductors wound in series into four contiguous cylinders. The solenoid is 405 cm long, with inner and outer radii of 156 cm and 171 cm, respectively. For a field of 4.75 kG, the current is 7325 A and the total heat dissipation is 1.8 MW.

The inner radius of the coil is covered by a heat shield which helps to isolate it thermally from the inner detector components. A flow of 40 liters per minute of temperature controlled water through the heat shield keeps the temperature within the central drift chamber stable to a few degrees. The magnetic field inside the cylindrical volume occupied by the drift chamber has been measured and fit to a set of polynomials in the coordinates r and z. Within the tracking volume the field is uniform to within 3% while the fit describes the magnetic field with an error of less than 0.1%. The magnetic field used in charged particle tracking is obtained from the fit normalized using the data from two Hall probes positioned at each end of the central drift chamber. The absolute error on the field strength is less than 0.1%.

5. LIQUID ARGON BARREL CALORIMETER

The central electromagnetic calorimeter of the Mark II is a lead/liquid argon sampling device with strip readout geometry. The calorimeter system consists of eight independent liquid argon cryostats enclosed in a common vacuum vessel. The system was designed and built as part of the Mark II at SPEAR [16].

5.1 Physical Description

Each module is $1.5 \times 3.8 \times 0.21$ m^3. The modules are arranged in an octagonal barrel outside the magnet coil. Together they cover the polar angle range of $47° < \theta < 133°$ and the full azimuthal angle except for $3°$ gaps between each pair of modules. The total solid angle coverage is 63.5%.

Each module contains a stack of alternating layers of 2-mm lead sheets and lead strips with the 3-mm gaps between them filled with liquid argon. The lead is strengthened with 6% antimony to minimize sagging. The strips are aligned either perpendicular to the beam axis to measure the polar coordinate θ, parallel to the beam axis to measure the azimuthal coordinate ϕ or at $45°$ relative to the other two sets of strips (labeled "U") to aid in track reconstruction. Table 2 gives the details for this design.

Spacing is maintained both between strips and between layers by ceramic spacers which contribute an overall dead space of 5%. In order to reduce the number of electronic channels many of the strips are ganged together, both from strip to strip in certain layers and from layer to layer. The ganging results in six interleaved readout layers and a total of 326 channels for each module. The ganging scheme is shown in fig. 14. There is an additional pair of 8-mm liquid argon gaps formed by 1.6-mm-thick aluminum sheets and strips in front of the lead stack to allow corrections to measured shower energy for radiative losses in the magnet coil. The strips are oriented in the ϕ direction and there are 36 in each module. Altogether, 1.86 radiation lengths of material precede the lead stack. Together this material and the calorimeter represent 16.0 radiation lengths of material at normal incidence.

5.2 Cryogenics System

The total volume of liquid argon in the modules is 6400 liters. The argon is not circulated; instead the modules are connected to a common storage vessel through gas phase transfer lines. With an insulating vacuum of 10^{-6} torr surrounding the modules, the major load for the cooling system is the compensation for heat losses

in the transfer lines. Temperature is maintained at approximately 85 K using liquid nitrogen refrigeration at the module shells. The system consumes 160 liters of liquid nitrogen per hour during normal operation.

5.3 Electronics

Charge produced through ionization in the liquid argon drifts to the readout strips in a field of 12 kV/cm. Each readout strip is impedance matched to a TIS75 FET through a small ferrite pot core transformer. The electronic noise is dominated by Johnson noise generated in the conduction channel of the FET and is minimized using a bipolar shaping amplifier [17] with a resolving time of 1.5 μs. The equivalent noise energy in the ganged readout channel varies from 0.3 to 1.5 MeV and is a function of the capacitance of the channel which varies from 0.9 to 8 nF. The preamplifiers and shaping amplifiers are mounted on the detector. RF shielding encloses the modules, the amplifiers, and the twisted-pair signal cables that run from the amplifiers to the electronics house.

Sample-and-hold modules (SHAMs [18]) follow the output voltage of the amplifiers and are gated to hold at the peak. The charge stored in the SHAMs is measured with BADCs [14]. The BADC in each of the six CAMAC crates performs pedestal subtractions, linear gain corrections, and threshold cuts. The maximum time for digitization and reduction of all data in a CAMAC crate is about 8 ms. Thresholds are normally set so that the noise occupancy is about 5%. After ten years of operation, the number of dead channels in the system (due to failing electronics or unrepairable internally shorted strips) is less than 1%.

5.4 Performance

The measured energy distribution from Bhabha scattering events at PEP is shown in fig. 15. The resolution is $\sigma/E = 4.6\%$, measured using the width of the distribution at the half maximum. However, the distribution is not Gaussian due to several reasons. Dead space in the calorimeter active volume creates a low energy tail, the size of which depends on the number of failing channels in the system.

Saturation in the readout electronics for the first active layer, used to correct for losses in the coil, further degrades the resolution for high energy electrons in the upgrade data sample. The gain in the amplifiers for the first layer has been reduced so that saturation will not affect running at the SLC. As fig. 15 shows, the Monte Carlo simulation [19], including the effects of dead space and saturation, roughly reproduces the distribution. The energy dependence of the resolution expected in future runs, without saturation, has been studied using Monte Carlo programs and is shown in fig. 16. The position resolution measured with the Bhabha scattering events is $\sigma_\phi = 3$ mrad and $\sigma_z = 0.8$ cm and both measurements are consistent with Monte Carlo simulation.

An inclusive electron production analysis [20] performed with data taken before the upgrade provides an example of the electron-hadron separation capability of the barrel calorimeter. Electrons were identified by comparing the momentum measured from a drift chamber track with the energy deposited in various groupings of layers in a narrow region around the extrapolated track. In hadronic events, the identification efficiency varied from 78% at 1 GeV/c to 93% at the highest momenta. The probability for misidentifying a hadron as an electron was typically 0.5% but could be as large as 3% for tracks of momentum below 2 GeV/c in the core of a jet. A more detailed discussion of the performance of the barrel calorimeter can be found in ref. 21.

6. THE ENDCAP CALORIMETER

The endcap calorimeters (ECCs) [22] were added to increase the electromagnetic coverage of the detector. These lead/proportional tube calorimeters are 18 radiation lengths (X_0) thick, and cover the angular region between approximately 15° and 45° from the beam axis. The first layer of the calorimeter is located 1.37 m in z from the interaction point. Together with the liquid argon calorimeter, they provide full electromagnetic calorimetry for 86% of the total solid angle (fig. 17).

6.1   Physical Description

Each ECC consists of 36 layers of 0.28-cm-thick lead (0.5 X_0) followed by a plane of 191 proportional tubes. The tubes are aluminum and have a rectangular cross section of 0.9×1.5 cm^2. The 191 tubes are glued together with epoxy to form an annular plane with inner and outer radii of 40 cm and 146 cm. A 50-μm-diameter Stablohm 800 (nickel-chromium alloy) wire is strung through the center of each tube. Alternating layers of tubes and lead are bonded together with 0.02-cm-thick epoxy-saturated fiberglass cloth to a flatness tolerance of 0.06 cm. The first twenty tube planes are oriented alternately in four different directions: vertically (X), horizontally (Y), canted $-45°$ (U), and canted $+45°$ (V). The remaining sixteen layers alternate between X and Y layers.

The gas (HRS gas) flows at slightly above atmospheric pressure through the proportional tubes at a rate of one volume per two days. The outer radius of the ECC consists of sixteen 0.16-cm-thick Lexan panels, which are made gas-tight with vinyl tape and epoxy.

To compensate for the variation of the gas gain with gas density, the temperature is measured with thermistors embedded in each ECC and the pressure is measured with transducers on the gas inlets and outlets. The variation of the ECC response is less than 2% after correcting for density changes. This stability is verified by the pulse height spectrum recorded by two small tubes that contain ^{55}Fe sources. These tubes, which are mounted on the inlet and outlet of the gas system for each ECC, are primarily used to monitor the gas quality.

6.2   Electronics

The signals from several tubes are ganged together to reduce the number of electronic channels to 1276 per endcap. Tubes are grouped in depth and in some cases laterally to give 10 interleaved measurements of the longitudinal shower development. The ganging follows a projective geometry so that all tubes in a channel lie approximately in a plane containing the interaction point.

The first half of the readout electronics [23] of the ECCs consists of charge-sensitive preamplifiers and shaping amplifiers mounted in electronics crates close to the detector. These are connected to the tube anodes by coaxial cables that carry both high voltage and signals. The second part of the system is a set of SHAM IIs and BADCs [18, 14] located in the electronics building. The system is calibrated by injecting a variable amount of charge into the front end of the preamplifiers. During readout, pedestal and gain corrections are applied to the data and a threshold cut is made.

6.3 Performance

One of the ECCs was tested in a positron beam and a pion beam prior to installation. Figure 18 shows the response of the ECC to pulses containing between one and five 10-GeV positrons. The five peaks are clearly distinguishable. The beam test data has been used to develop algorithms that reject 99% of isolated pions while retaining 95% of electrons at a momentum of 5 GeV/c.

A study of Bhabha scattering events in the ECCs at PEP gave an energy resolution of $22\%/\sqrt{E}$ (E in GeV). Since the PEP run there has been a substantial decrease in the number of dead channels and an improvement in the gas tightness of the system, so this resolution may well improve. A position resolution of 0.27 cm in both the x and y directions was measured.

A minimum-ionizing particle traversing an ECC deposits energy equivalent to a 380 MeV photon. The readout electronics are quiet and sensitive enough to allow this track to be reconstructed in the presence of low backgrounds.

7.   MUON SYSTEM

7.1 Physical Description

The Mark II muon system is made up of layers of hadron absorber and proportional tubes mounted on four sides around the central detector. Each wall of the muon system consists of four alternating layers of iron and proportional tubes.

The solid angle coverage is 45% at the outermost layer, and the total number of interaction lengths is 7.3. The tubes in the innermost layer are oriented perpendicular to the beam direction to measure the polar coordinate of a track, while the tubes in the outer three layers are oriented parallel to the beam direction to measure the azimuthal coordinate. The thickness of the muon absorber and the distance of each plane of chambers from the interaction point are shown in table 3.

Each muon layer consists of extruded aluminum modules made up of eight triangular tubes as illustrated in fig. 19. The wire spacing of 2.5 cm was chosen to approximately match the expected multiple-scattering deviation for a particle passing through each layer of absorber. Each tube contains a 45-μm wire of gold-plated tungsten held at a voltage of 2.0 kV. The gas used in the tubes is a mixture of 95% Ar and 5% CO_2 at a pressure slightly above atmospheric.

There are 3264 channels (408 modules) in the entire muon system. Signals from each wire are discriminated at a level of 2 mV and stored in a shift register array for readout in a serial chain upon receipt of a trigger signal. Since it is a digital system, no calibration is necessary. Pulsing the high-voltage line and reading out all channels allows the integrity of the readout system to be checked at the beginning of each data-taking run.

7.2   Performance

The muon system provides an identification efficiency of typically greater than 85% for incident tracks with momentum greater than $\approx$ 1.8 GeV/c. Below this momentum all charged particles are expected to range out before the fourth layer, due to dE/dx losses. Chamber inefficiencies are $\simeq 1 - 2\%$ per plane.

To reject background from hadronic punchthrough and muonic decays of pions and kaons in multihadronic events, we typically require an extrapolated drift chamber track to have associated hits in all four layers. These hits are required to be within a search region of twice the expected rms deviation due to multiple scattering and track extrapolation error. Using this strict requirement, the observed

22

identification efficiency for muons in multihadronic events in the pre-upgrade data sample was $\simeq 85\%$. The observed per track muon misidentification probability was $\simeq 0.5\%$ at low momenta, rising to $\simeq 0.8\%$ at 10 GeV/c. At SLC energies the increased track densities and momenta will lead to more hits in the muon system. However, the misidentification probability is not expected to be substantially higher than at PEP as the better position resolution of the new drift chamber leads to a smaller search region in each muon system layer.

8. LUMINOSITY MONITORS

Two detectors whose main function is to measure precisely the integrated luminosity have been built especially for SLC running. The Small-Angle Monitor (SAM) covers the angular range 50 mrad $< \theta <$ 160 mrad, and the Mini–Small-Angle Monitor (Mini–SAM) covers 15 mrad $< \theta <$ 25 mrad. Both detectors use small-angle Bhabha scattering to measure luminosity, and both detectors provide rejection of radiative Bhabha backgrounds in neutrino-counting experiments.

8.1   Small-Angle Monitor

8.1.1   Mechanical design

The SAM consists of a tracking section with nine layers of drift tubes and a sampling calorimeter with six layers each of lead and proportional tubes (see fig. 20). Each layer of lead is 13.2 mm thick, giving a total of 14.3 radiation lengths. There are four SAM modules, two on each side of the interaction point (IP). The front face of the SAM is 1.38 m from the IP. Pairs of SAM modules are assembled around the beam pipe as is shown in fig. 21. The layers are arranged in three different orientations. The tubes in the first layer (Y) are horizontal and the other two layers (U,V) are rotated $\pm 30°$ from Y when looking at the front face of the SAM from the IP. For both the tracking and calorimetry layers, the pattern of layer orientation is a series of repeating triplets YUV as seen from the IP.

23

Both the drift and proportional wire planes are constructed from square aluminum tubes 9.47 mm wide with a wall thickness of 0.25 mm. The sense wire in each tube consists of 38-μm-diameter gold-plated tungsten. Positive high voltage is applied to the sense wires with respect to the tube wall, which is at ground potential. This voltage is 1800 V for the tracking tubes and 1700 V for the calorimeter tubes. Each of the four SAM modules contains 30 tubes per layer, giving 270 tracking and 180 calorimeter cells per module. All tubes operate with HRS gas. Since the gas gain depends strongly on the density, the temperature and pressure of the gas are monitored by thermistors and transducers mounted on the SAM modules.

8.1.2 Electronics

The electronics for the tracking part of the SAM consist of LeCroy LD604 amplifier/discriminators and TACs [18] that are read out by BADCs [14]. The calorimeter part is instrumented with custom-designed amplifiers and the signals are stored in SHAMs [18] which are also read out by BADCs.

Calibration pulses are injected at the input to the amplifier with variable time delays and constant pulse height for TACs and with constant time delay and variable pulse heights for SHAMs. The resulting signals are fit linearly or quadratically to extract the calibration constants that are then stored in the BADCs for subsequent application to incoming data.

8.1.3 Performance

One of the four identical SAM modules was tested in a beam of positrons at 5, 10 and 15 GeV. The measured tracking resolution was 250 μm, which yields an intrinsic angular resolution for Bhabha tracks of 0.2 mrad assuming the SLC interaction point is known. The measured energy resolution in the range of 5–15 GeV can be parametrized by $\sigma/E = 45\%/\sqrt{E}$ (E in GeV) for showers near the center of the SAM active area. The resolution worsens somewhat at the edges because of radial shower leakage. Longitudinal shower leakage increases from 9% at

5 GeV to about 22% at 50 GeV, and fluctuations in this leakage degrade the energy resolution. The position resolution for locating showers with just the calorimeter section of the SAM is 5 mm. This number is used for matching tracks with showers and also represents the precision with which photons entering the SAM can be located. The SAM Bhabha rate is estimated to be roughly 20% higher than the visible Z^0 rate. The expected systematic error on the luminosity measurement is $\approx 2\%$.

8.2 Mini–Small-Angle Monitor

8.2.1 Mechanical design

The Mini–SAM surrounds the beam pipe at 2.05 m on either side of the IP (see fig. 22). It is composed of six layers of 0.64-cm-thick scintillator (BC404 [24] plastic) interleaved with 0.79-cm-thick tungsten slabs providing 15 radiation lengths in total thickness and resulting in an expected energy resolution of $35\%/\sqrt{E}$ (E in GeV). The first scintillator layer is preceded by two layers of tungsten (4.5 radiation lengths) as a preradiator. The layers are divided into four equal azimuthal segments, each read out with a Hamamatsu R2490 photomultiplier tube viewing a wavelength shifter bar running the length of each azimuthal segment. Angular acceptance windows are sharply defined by 5.08-cm-thick conical tungsten masks (15 radiation lengths). These masks are asymmetric; this reduces changes in acceptance due to motion of the interaction point, motion of the center-of-mass of the electron-positron system and bremsstrahlung. The angular acceptance is 15.2 mrad $< \theta <$ 25.0 mrad on one side of the IP, and 16.2 mrad $< \theta <$ 24.5 mrad on the other side.

8.2.2 Electronics

The Mini–SAM readout electronics are described below in the chapter on small electromagnetic shower detectors. The Mini–SAM is read out on every trigger to monitor noise and to provide electron detection for vetoing events in studies such as neutrino counting. In addition, coincidences are scaled and read out at four-minute

intervals to provide an online luminosity measurement. Signals are also sent from the Mini–SAM to the trigger logic to provide an additional Bhabha trigger.

8.2.3 Performance

The Mini–SAM as installed was not tested in a beam; however, a very similar prototype was placed in a 10 GeV e^- test beam, and these tests confirmed EGS [25] shower studies of both the shower profile and the predicted performance of the tungsten aperture masks. A test of the integrity of the Mini–SAM has been done using cosmic rays. The observed cosmic ray signals have been used to set an approximate energy scale for the device.

To make a measurement of the luminosity, small-angle Bhabha pairs must be detected above a potentially large background from the SLC beams. A Bhabha pair is defined by back-to-back coincidences of discriminated signal sums of adjacent azimuthal segments as shown in fig. 23. The rate of accidentals is measured by delaying signals from the south Mini–SAM until the next beam crossing and forming coincidences with undelayed signals from the north monitor, and by forming coincidences between azimuthal segments which are not back-to-back. The tungsten masks defining the angular acceptance result in a Mini–SAM Bhabha rate of approximately eight times the total estimated visible Z^0 rate at $\sqrt{s} = M_Z$. A luminosity measurement with a 10% statistical error at a luminosity of 10^{29} cm^{-2} s^{-1} would therefore take 1.1 hours.

9. SMALL ELECTROMAGNETIC SHOWER DECTECTORS

The requirements of hermeticity and low-angle coverage have prompted the design and construction of four small detector systems which provide shower counter coverage in the solid angle regions not covered by the main calorimeters. Figure 22 shows the small-angle coverage in the 15–250 mrad region provided by three of the systems described below along with the SAM and the Mini–SAM. The functions of these detectors include luminosity and noise monitoring as well as detecting electrons and/or photons escaping through cracks.

The photomultiplier tube signals from these four detector systems and the Mini–SAM are read out and processed as a group, using a BADC–SHAM IV combination [14, 26] similar to that used by the liquid argon barrel and endcap calorimeter systems. Calibration and a check of system integrity is performed by flashing LEDs mounted in detector elements. The brightness of the LED flash is varied under CAMAC control by changing the time width of the LED driving pulse. Three CAMAC-controlled LeCroy 4032A 32-channel high-voltage units are used to supply the photomultiplier tube high voltages.

9.1   Catcher/Mask Plug

The Catcher/Mask Plug is located between 25 and 40 mrad in θ and surrounds the beam pipe 1.02 m on either side of the interaction point. It consists of two layers of SCSN–38 scintillator separated by a layer of tungsten, all in the shape of flat annuli. Light is collected by wavelength shifter bar wrapped around the outer radius of the detector in 180° segments. Optical fibers at one end of each wavelength shifter segment lead the light out to Amperex XP2262 photomultiplier tubes mounted outside of the solenoidal magnetic field volume.

The Catcher/Mask Plug acts as a crude luminosity monitor, as it detects Bhabha scattering events at a rate of one-third of that of the Mini–SAM. More importantly, in conjunction with the active mask, it is used to veto radiative Bhabha events which are a background to neutrino counting.

9.2   Active Mask

The Active Mask is a Čerenkov detector located inside a tungsten synchrotron radiation mask positioned 63.5 cm from the interaction point. The detector is comprised of three cylindrical layers of high purity silica optical glass fibers (2400 fibers per mask, each fiber 230 μm in diameter) sandwiched between layers of lead, each about 0.14 cm thick, which act as a preradiator. The resulting electromagnetic showers radiate Čerenkov light in the glass fibers which also transport the light from the detector. Upon leaving the mask, the fibers are collected into bundles which

27

are led along the beam pipe and out of the high magnetic field region. Each fiber bundle is then viewed by an Amperex 2252H photomultiplier tube. The outer layer of optical fibers is read out independently of the inner two layers to allow a coincidence to be made.

The Active Mask provides coverage for the region between the SAM and the Mask Plug (30 mrad $< \theta <$ 50 mrad), and also acts as a background monitor for off-energy electrons that strike the beam pipe. Beam test data for a prototype showed a yield of 1 or 2 photoelectrons per GeV of incident electron energy.

9.3 Endcap Veto Counter

The purpose of the Endcap Veto Counter is to detect energetic electrons and photons (2–50 GeV) which could otherwise pass undetected between the SAM and the endcap calorimeter. Its efficiency is predicted by computer simulation to be greater than 99% in this energy range.

The Endcap Veto Counter is an annular electromagnetic shower counter located between the endcap calorimeter and the endcap door. It is located at a distance in z of 1.9 m from the interaction point and covers an angular region of 150–250 mrad in θ. The counter is composed of four alternating layers of lead and scintillator resulting in a total of 4.6 radiation lengths of material. Eight wavelength shifter bars collect the light signal from equal sections of the outer edges of the scintillator layers. The light is then transmitted through optical fibers to Amperex 56AVP photomultiplier tubes. By taking a weighted average of photomultiplier signals, a typical ϕ resolution of $\sigma_\phi = 10°$ was measured with cosmic rays; the same resolution is expected for a 50 GeV electron.

9.4 Liquid Argon Hole Taggers

For $|\cos\theta| < 0.7$, at each junction between liquid argon calorimeter modules, a 3° region in ϕ is not instrumented with calorimetry. Liquid Argon Hole Tagger counters are mounted on the outside surface of the liquid argon cryostat to fill

in these "cracks" and to detect photons escaping through them. They also provide a very crude energy measurement to assist in the correction of the energy measurement of showers near or in cracks between modules.

Each counter consists of a slab of 2.5-cm-thick scintillator, 20 cm wide and 1.65 m long, at a radius of 2.4 m from the interaction point. Each counter is faced with 1.9 cm of lead preradiator, which, along with other detector elements, gives a total of 6 radiation lengths of material preceding the scintillator. A Monte Carlo simulation implies that this should result in a detection efficiency of greater than 98% for electrons and photons with energies above 1 GeV. The scintillator is viewed at both ends by Amperex XP2230 photomultiplier tubes. A single hit position resolution of $\sigma_z = 35$ cm is obtained for cosmic rays by comparing relative signal pulse heights at each end. Due to interference from cryogenic plumbing, individual counters could not extend the entire length of the liquid argon cryostat, so additional shorter hole tagger counters are placed to cover the remaining uninstrumented region. The crack between the modules at $\phi = 270°$ could not be instrumented due to physical constraints.

10. TRIGGER SYSTEM

The trigger used for running at the SLC combines a modification of the trigger used at PEP with new FASTBUS-based logic. At SLC the beam crossing rate can range between 10 and 180 Hz, although it is not expected to exceed 120 Hz during the Mark II experiment. Since this allows sufficient time to run the trigger logic on every beam crossing, beam crossing signals supplied by the accelerator provide the primary trigger. These signals also provide a highly accurate timing reference for the electronics systems of the detector components. The interface between the trigger logic and the host VAX is provided via CAMAC by the Master Interrupt Controller (MIC) module.

10.1 Data Trigger

There are three components of the normal data trigger. They use information from the central drift chamber, electromagnetic calorimeters and small-angle monitors. Each component operates independently and provides a degree of redundancy to assist in monitoring the performance of the other components. This redundancy is also used to measure their relative triggering efficiencies.

10.1.1 Charged particle trigger

The charged particle trigger uses a fast track-finding processor [27] to count the number of charged tracks traversing the drift chamber. Pattern recognition can be done with up to 12 detector layers; currently, the 12 layers of the central drift chamber are used. No information about the z-coordinate is used. This design requires approximately 60 μs to count the charged tracks.

A drift chamber cell is considered "hit" when at least four of the six sense wires in the cell have signals detected by the TDCs. (The number of wires which determine a hit is programmable.) This requirement is a powerful means of rejecting backgrounds which do not produce track segments. Requiring a track to traverse more than half a cell produces a geometrical inefficiency of less than 0.5% for tracks of $p_t \gtrsim 1$ GeV/c.

The pattern of hits in each layer is loaded into a shift register and transferred serially into special hardware curve-finding or "curvature" modules as shown in fig. 24. Each curvature module is programmed to identify patterns of hits falling within a specific range of radii of curvature called a road. These modules currently require hits in at least five axial and five stereo layers to define a track, but can also be programmed to require any pattern of layers.

Track counters are used to record the total number of tracks found as well as the azimuth of each track. All tracks found by all curvature modules within $\sim 10°$ in azimuth of each other are counted as a single track. The total number of tracks found is encoded into two bits which are passed to the MIC for the trigger decision.

30

10.1.2 Calorimeter energy trigger

The calorimeter energy trigger uses a table of constants stored in a memory module to find events with topologies of interest. The event topology is defined by thresholds placed on the energy deposited in the liquid argon, endcap and SAM calorimeters, and in small-angle counters.

A programmable Memory Logic Module (MLM) encodes 32 input bits into two output bits which are returned to the MIC; this requires a few hundred nanoseconds. The MLM uses information from the SAM, Mini–SAM and active mask to form a low-angle Bhabha trigger for luminosity monitoring, while calorimeter information is used for the Total Energy Deposition (TED) trigger. The TED trigger uses groups of eight adjacent channels (strips in the liquid argon calorimeter; proportional tubes in the endcap) which are summed at the detector. The sum representing each LA module is compared with a threshold voltage by a strobed discriminator [28]. The sum for each endcap is fed into two discriminators with different thresholds. The value of these thresholds is ultimately limited by the maximum trigger rate permitted by the data acquisition system.

10.1.3 SSP-based software trigger (SST)

The SST was more recently designed to duplicate the capability of the TED trigger and, in addition, to provide new software flexibility for improving both its noise sensitivity and pattern recognition characteristics. The redundancy available to the two triggers can also provide an important cross check for calorimeter triggering. A SLAC Scanner Processor (SSP) is the component of the SST which processes the calorimetric data in a much more flexible manner than the TED trigger. Copies of the LA and EC trigger sums are made by summing/buffer boards which are then digitized by LeCroy 1885N FASTBUS ADCs. In one pass the SSP reads out the ADCs and defines "hits" based on three software thresholds. Trigger algorithms then find calorimetric "towers" (clusters of energy which point to the IP) by using the hits to index a table of precalculated patterns. (The complexity

31

of the algorithm is constrained only by the time available between beam crossings.) Since only the energies of the channels contributing to a tower are summed, the SST eliminates noise from other channels in the modules. More details on the SST system may be found in ref. 29.

In addition to the calorimeters, the SST reads out various monitors through its ADCs. There are 48 ionization chambers in the last section of the SLC beamline, and 16 proportional tubes along the beamline in the experimental hall (and inside the Mark II). An increase in the signals from these monitors is indicative of various accelerator-related problems such as klystron tube and magnet failures or mis-steering of the beams.

10.2 Cosmic Ray Trigger

Cosmic ray events are needed for debugging and performance evaluation of individual detector components, including the charged particle trigger. Cosmic rays can be recorded between beam crossings or during dedicated cosmic ray runs. The trigger is either the normal charged particle trigger or a coplanar track finder (CTF) that is used to look specifically for back-to-back tracks. The CTF uses two curvature modules to estimate the azimuth of tracks, and returns a bit to the MIC when a pair of tracks is found that are coplanar to within $\sim 11°$. The TOF system provides the absolute time measurement of the cosmic ray that is required by the drift chamber reconstruction software.

11. EXTRACTION LINE SPECTROMETER

In order to determine the center-of-mass energy (E_{cm}) at the SLC interaction point (IP), precise measurements of the beam energies (E_{beam}) for both the e^- and e^+ beams are essential. To meet the resolution goal of $\sigma_{E_{cm}}/E_{cm} < 0.05\%$, precision spectrometers have been installed [30] in the SLC extraction lines, 150 m downstream of the IP in both beam lines.

11.1 Spectrometer Description

Figure 25 shows a conceptual design of the extraction line. In the line, the $e^{\pm}$ bunch travels through a string of three dipole magnets (B31, B32, and B33). Magnet B32 is a well-measured spectrometer magnet (set at $\int Bdl = 30.5$ kG · m when E_{beam} is 50 GeV) which bends the beam by an amount proportional to $\int Bdl/E_{beam}$. Magnets B31 and B33 bend the beam perpendicular to the bend direction of B32 and cause the beam to emit two 5-cm-wide swaths of synchrotron radiation. Synchrotron light detectors located at the beam focal point (approximately 15 m from B32) measure the distance between these swaths (approximately 27 cm) and thus the angle through which the beam has been bent by magnet B32. Combining this information with the strength of the magnet allows a determination of the energy of the beam. Analysis of the thickness of the synchrotron stripe yields the energy spread of the beam.

11.2 Magnetic Field Monitoring

Two high-precision, absolute methods were used to make a determination of the magnetic strength of the B32 magnets before their installation in the extraction line. The first measured $\int Bdl$ directly by moving NMR probes along the length of the magnet, measuring B and dl for each step. In the second method, $\int Bdl$ was measured by monitoring the voltage induced on a moving loop of wire. These methods are described in detail elsewhere [31]. The techniques agreed to better than 0.008%.

The absolute measurements were used to simultaneously calibrate three online methods of determining the spectrometer strength: a flip coil, NMR probes, and current monitors. Figure 26 shows a cross section of the magnet with these devices installed in the gap. Agreement between the flip coil and NMR probes is better than 0.01%.

11.3 Detection of Synchrotron Radiation

The bend magnets cause the beam to emit intense swaths of synchrotron radiation with a critical energy [32] of approximately 3.0 MeV. An energy spread of 0.2% in the bunches causes the stripe from B33 to be dispersed by about 540 μm at the detector plane. Two independent detectors have been built to detect the separation and width of the two synchrotron swaths: a Phosphorescent Screen Monitor (PSM) (fig. 27) and a Wire Imaging Synchrotron Radiation Detector (WISRD), which is not yet in operation (see sec. 13.4).

The PSM consists of two identical target and camera systems to monitor both stripes simultaneously. An Invar [33] support structure holds both targets and fixes the distance between them. Each target consists of an array of 100-μm-diameter fiducial wires with center-to-center spacing of 500 μm and a phosphorescent screen that emits light where struck by the synchrotron beam [34]. The individual wires and the spacing between the two arrays were measured on precision optical comparators to an accuracy of better than 10 μm. A camera system records both the fiducial wires and the synchrotron stripe which runs parallel to them. The video frame is digitized and compressed by a DSP Technology 2030/4101 signal averager into a one-dimensional array (perpendicular to the wire direction) before readout. Ultimate system resolution has been measured to be better than 25 μm and readout rates up to SLC design repetition rate (180 Hz) are possible.

11.4 Performance

In addition to the errors on the measurement of $\int B dl$ and the separation between the synchrotron stripes, there are other contributions to the error on measuring E_{beam}. These contributions include the survey of distance and misalignments between B32 and the detectors, and misalignments between bend magnets. Combining these contributions in quadrature yields an estimated total error on E_{beam} of 15 MeV. However, knowledge of the average energy of the beam bunch does not necessarily determine the luminosity-weighted E_{cm} at the IP. Complete understanding of correlations between particle position and energy in the two colliding

34

bunches is essential to limit the systematic error on the energy measurement. Preliminary measurements of E_{beam} have been made in both extraction lines using the PSM's and the magnetic monitors. An absolute accuracy of 35 MeV on $E_{e\pm}$ has been achieved.

12. DATA ACQUISITION SYSTEM

Data acquisition for the Mark II detector is performed by a system of software and hardware elements. The software consists of a number of independent processes running on the host VAX 8600 under the control of the VMS operating system. Each process performs a primary function and communicates with the other processes via shared memory (global) variables, shared instructions and a form of interprocess communication known as event flags. These functions include: reading CAMAC data; reading FASTBUS data; merging of raw data with results from online event tagging; tape logging of data records; disk logging of tagged data records; monitoring of detector performance, electronics and environmental status; online analysis and histogramming; and operator control of the experiment.

All data from the detector are channeled into the VAX through either the CAMAC or FASTBUS interfaces. The amount of data read per event varies with the event topology. A Z^0 decaying into 20 charged particles will typically result in approximately 50 kbytes of data.

The CAMAC interface is a UNIBUS-based microprocessor system called the VAX CAMAC channel or VCC [35]. This system is capable of transferring 24 bits of data every 2 μs. Generally, however, only the least significant 16 bits are used resulting in a transfer rate of 1 Mbyte/s. The VCC operates a parallel branch serving two system crates [13]. These system crates contain a total of 11 branch drivers which connect with the 44 data acquisition crates. Event triggers are generated within the CAMAC system and are posted as AST (Asynchronous System Trap) interrupts on the VAX. CAMAC event acquisition consists of multiple VAX reads of individual BADC memories and other general instrumentation modules.

The FASTBUS system interface consists of two parts. The first part is a DEC DR–780 32-bit parallel port which connects the VAX SBI (Synchronous Backplane Interconnect) with a DDI (DR–32 Device Interconnect) cable. This DDI cable connects with another interface [36] which provides access to a FASTBUS crate segment through a simple buffer module, BAFFO (see fig. 28). The combined interface supports interrupt messages and block transfer data rates of approximately 5.5 Mbyte/s between the VAX and an SSP. Two FASTBUS crates running in parallel serve as system crates. One system crate contains five system SSP modules that each in turn control one of the five FASTBUS cable segments connected to the 25 remote data acquisition crates [37]. Each remote crate contains a single SSP acting as an intelligent crate controller and data processor, along with the data acquisition modules. The second system crate contains a pair of SSPs managing a sixth cable segment used for a future project involving online data processing (see sec. 13.5). Event acquisition begins with remote crate SSPs performing local data readout and processing, then reporting to the appropriate system SSP. The master system SSP acts as an event builder, collecting the entire FASTBUS component of an event into its own local memory before interrupting the VAX. In this way, the FASTBUS system is able to buffer several events before being read out. The VAX then performs a single block read from the master system SSP.

Event acquisition proceeds in the following way. A signal is generated at every beam crossing (e.g., 8.3 ms at 120 Hz). This signal starts the trigger logic (see sec. 10) and BADC processing which requires approximately 8 ms. Note that no dead time is introduced as a result of running the trigger logic for every beam crossing. The VAX reads data from the entire CAMAC system and awaits a signal from the master system SSP that the FASTBUS system is ready to accept the next event. When the signal is received the trigger is reset. FASTBUS data is subsequently read into the VAX, combined with the CAMAC data and a simple event tagging algorithm is executed. The event is then placed into a global buffer where consumer processes, such as the online analysis program, sample the com-

plete events. The tape logging process is the final consumer of all events and, after logging is completed, removes the event from the buffer.

13.   FURTHER IMPROVEMENTS

There are several projects which improve the Mark II detector that are in the process of being installed. They will be briefly described here.

13.1   Silicon Strip Vertex Detector

The Silicon Strip Vertex Detector (SSVD) consists of 36 independent detector modules housed in two hemi-cylindrical structures that attach to the beam pipe at the interaction region. The modules are grouped into three radial layers (starting at 2.8 cm from the beam axis) that provide a solid angle coverage comparable to the central drift chamber (see fig. 29). The strips are oriented parallel to the beam axis and hence track position is measured only in the $r - \phi$ plane. The detecting element in each module is a single-sided, 512-strip silicon detector of 300-μm thickness. Additional properties of the detectors are given in table 4.

The problem of reading out a high density of silicon strips in the limited space available for the vertex detector in the Mark II was solved with the development of a custom 128-channel VLSI chip (the "Microplex") [38]. The circuit integrates and stores the charge deposited on a strip and multiplexes the analog signal onto a serial bus. In the construction of a module, four chips are wire bonded to a detector as shown in fig. 30 so that all 512 strips can be read out. The module also includes a hybrid circuit which provides control signals, a switchable capacitor bank for the power, and a differential amplifier and line driver for the analog output signals. Thin flexible cables are used to carry signals to both ends of the modules and from the hybrids to the readout chips. The analog output signals are sent to an intelligent digitizer, the BADC [14], which does online pedestal updating and subtraction, common mode correction and cluster finding.

37

The 36 modules are housed in two hemi-cylindrical structures each consisting of two slotted aluminum endplates connected by an inner and outer beryllium shell. A spring fixture on either end of the modules holds them in the endplate slots. This system sets the parallelism of the detector strips to better than a milliradian, a requirement that follows from the z resolution of the central drift chamber. The precise determination of the relative alignment of the modules is obtained by optical measurements during assembly, and later by a method that uses a beam of collimated X-rays. Once the SSVD is installed in the center of the Mark II detector, it will be aligned as a whole relative to the other tracking chambers using tracks from beam-beam interactions. Also, a capacitive sensor system has been attached to the outer shells of the SSVD to monitor any movement of the beam pipe, and hence the SSVD, relative to the drift chamber vertex detector.

Tests of the modules with X-ray sources and particle beams show that they have a spatial resolution, σ, of better than 5 μm, a two-track separation of approximately 150 μm and a single-channel rms noise level 19 times smaller than the signal corresponding to the most probable energy loss of a minimum ionizing particle incident at 90° [39]. This signal-to-noise ratio allows a threshold cut that gives essentially 100% detection efficiency with a negligible number of noise hits. Combining hits from high momentum tracks in the central drift chamber with those from the SSVD yields an impact parameter resolution for high momentum tracks comparable to σ. Multiple scattering in the material of the SSVD and beam pipe worsens this resolution at low momentum. The resultant error can be approximated by $\sigma + 36/p$ (μm) for momenta, p, of less than 8 GeV/c.

13.2   Drift Chamber Vertex Detector

The Drift Chamber Vertex Detector (DCVD) has been designed to provide vertexing information that is both independent of and complementary to the information provided by the Silicon Strip Vertex Detector. The DCVD alone is designed to provide an impact parameter resolution of 20 μm for high momentum tracks, and submillimeter double-track resolution. The powerful pattern recogni-

tion of the DCVD will provide an important aid to hit assignment in the SSVD, particularly in a high noise environment. The DCVD will also improve the charged particle momentum resolution, enhance dE/dx particle identification, and improve the noise rejection of the charged particle trigger.

The active volume of the DCVD extends from 5 to 17 cm radially and 55 cm axially, covering 85% of 4π in solid angle at the outer radius of the detector. The chamber is divided into 10 axial cells which, as for the SSVD, provide information only in the r–ϕ plane (fig. 31). To allow resolution of the left-right ambiguity, as well as to ensure that radial tracks do not spend their entire length close to a wire plane, each cell is tilted so that the inner edge of the sense plane is at an angle of 15° from radial.

Each cell contains a plane of 40 sense (anode) wires, at a voltage of +3 kV, alternating with grounded field shaping wires (fig. 32). These sense planes are sandwiched between 'grid' planes at −0.5 kV that provide the electrostatic stability of the sense wires and serve to focus the drifted electrons onto the sense wire. A drift field of 2.3 kV/cm, uniform to within 0.1% over two-thirds of the active volume, is provided by planes of cathode wires, with voltage graded between −3 kV at the inner radius of the detector to −12.5 kV at the outer radius. The longest drift distance, between the cathode and sense planes at the outer edge of the active volume, is about 5.5 cm.

The wires are supported by Macor wedges, which are affixed to circular aluminum endplates which form the ends of the active region (fig. 31). Within each plane, wire position was established by grooves machined into two Invar cylinders, which were used to hold the wires in place as they were epoxied to the Macor wedges. In this way, tolerances of ±2 μm were obtained for wires within a single plane, and of ±15 μm for the offset between planes. A more detailed description of the cell construction can be found in ref. 40.

The chamber volume is sealed by two aluminum pressure heads, surrounded by an outer shell of aluminum and an inner core of beryllium. Including the beam

pipe and SSVD, the material between the interaction point and the active region of the chamber comprises a total of about 0.03 radiation lengths.

To achieve the best spatial resolution, the DCVD gas (92% CO_2, 8% ethane) is run in the unsaturated regime, which provides low electron diffusion and a slow (6 μm/nsec) drift velocity. A sufficient electron lifetime, in excess of 30 μsec, is obtained by use of an Oxisorb filter, which reduces oxygen contamination to less than 1 ppm. In addition, chamber performance in a slow gas is sensitive to the density of the gas, requiring the use of feedback-controlled pressure and temperature regulation. The latter is implemented by a computer-controlled water bath (Haake N2-R), which circulates water through a 6-mm aluminum tube around the two pressure heads and the outer shell of the detector. The temperature field is monitored by 48 thermistors surrounding the active volume of the detector. This system is expected to keep the temperature of the detector constant and spatially uniform to within 0.1° C. Chamber pressure is regulated to within 0.7 $\times$ 10^{-3} atmospheres by a Datametrics 1501 Pressure Controller.

Electronic readout and processing begins with fast integrating Radeka hybrid preamps (BNL Hybrid IO-354), which are mounted onto feed-throughs at the pressure head, and enclosed in aluminum Faraday cages. The signals then travel to postamplifiers and FADCs [41], both of which are similar to the corresponding electronics of the central drift chamber (discussed in sec. 2.2). Because of the long drift times associated with the low drift velocity, the FADC digitization window has been increased to 1024 10-nsec buckets.

Tests have been conducted [42] on a prototype chamber with a single sense/grid plane containing 22 sense wires, a drift field of 1 kV/cm/atmosphere, and using 92% CO_2, 8% Isobutane at 3 atmospheres. The single hit spatial resolution σ was found to be dominated by the electron diffusion in the pressurized thermal gas, and can be parametrized by:

$$\sigma^2 \ [\mu m^2] \ = \ 16^2 + D \cdot 23^2 \quad ,$$

where D is the drift distance in centimeters.

13.3   Muon System Upgrade

13.3.1   Physical description

The Mark II muon upgrade provides additional coverage on the front and rear of the detector, as shown in fig. 1. The "facades" increase coverage for muon detection to $|\cos\theta| \approx 0.85$, an increase of 15% in solid angle.

A schematic drawing for a lower facade can be seen in fig. 33. The facade is attached to the end flux return iron and is 2.7 m in z from the IP. A particle coming from the interaction point will penetrate the endcap electromagnetic calorimeter, the flux return and 30 cm of lead, a total of 6.0 interaction lengths, before it reaches the first detection chambers. After passing through an additional 20 cm of iron there is a second layer of chambers at the rear of the facade. This set of chambers is shielded from synchrotron radiation by a 3-cm iron plate.

The chambers are constructed from the same aluminum extruded stock as the original Mark II muon system (see fig. 19). The triangular chambers are grouped together to form modules, with 72 modules (576 chambers) in all. Both layers in a facade have wires oriented in the horizontal direction. The construction and assembly followed the same steps as the central muon system described in sec. 7.1. This system does differ from the original system in that HRS gas is used in the chambers.

13.3.2   Electronics

Signals from a muon module (8 channels) are carried on 90-Ω AMP ribbon coaxial cables to half-size VME cards that use Signetics NE592 amplifiers with gains of 200. The amplified signals pass to VME crates, mounted on the plate on the rear of the facade, containing 16-channel TDC cards in VME format. Common

41

clock, clear and threshold signals are supplied to each VME crate and distributed on a local timing bus. The clock period is 13 ns.

The system contains a total of four crates with TDCs, all read from a common master crate through VME Micro Systems Model 485 long-line extenders. Command input and event readout is handled by an AT&T 321SB computer located in the master crate. The event information is sent to a FASTBUS FIFO module over a 32-bit parallel path at RS422 levels. The FIFO module is located in one of the data acquisition system FASTBUS crates.

The electronics system will provide drift time information in addition to the wire number that was hit. For a small test module, the precision of the position measurement is about 250 μm. A precision of 500 μm in the installed system is estimated.

13.3.3 Muon identification

The implementation for muon identification in the upgrade will follow the scheme used by the main system. A drift chamber track is first extrapolated to the muon facade. An expected rms deviation due to multiple scattering is calculated and a search region of twice the deviation (a road) is defined around the extrapolated track. To be identified as a muon, the track must have hits in both layers in the defined road. Additionally, the track hits must pass an angle cut and a position-angle correlation cut. Monte Carlo simulations have shown that the efficiency for muon identification is comparable to the existing muon system. The punchthrough probability for pions and kaons can be parameterized as $0.055 \times p\%$, where p is the momentum of the track in GeV/c.

13.4 Wire Imaging Synchrotron Radiation Detector (WISRD)

The WISRD will provide redundancy and a check on the systematic error in the measurement of the position of the synchrotron stripes in the extraction line spectrometer. In the WISRD, there are two targets held in position by an Invar support structure (fig. 34). The targets consist of arrays of 75-μm-diameter

copper wires spaced 100 μm apart (center-to-center). The wires are held in place in a ceramic card which is glued to the support structure. Incident synchrotron radiation ejects electrons from the wire via Compton scattering. The residual charge (calculated to be 200 fC with $10^{10}e^{\pm}$ in the beam bunch) is sampled by a charge sensitive preamplifier (LeCroy HQV820), then amplified, shaped, and digitized. Design resolution of this system is 25 μm with a readout rate of 180 Hz.

13.5 Online Processing

The 3081/E [43] is a specialized reduced instruction set processor, developed jointly by SLAC and CERN, to provide significant numerical computation capability at a reasonable cost. The name derives from its emulation of the instruction set of an IBM mainframe computer. It can realize most FORTRAN 77 directives including double precision floating point arithmetic operations.

13.5.1 Hardware

The hardware architecture is characterized by a modular structure, permitting separation of functions and reduction of control logic complexity. There are four distinct execution boards performing computations involving integer arithmetic, floating point addition, floating point multiplication, and floating point division. Each processor contains up to 7 Mbytes of fast static memory (55-nsec access time) and the processor cycle time is 120 nsec.

13.5.2 Software

Programs for execution on the processor are prepared by a software procedure called the Translator, resident on the IBM mainframe computer. This procedure reads IBM object code, translates it to processor microcode, and links elements together to form an absolute load module. The Translator eliminates the need for a complex hardware interpreter to decode the IBM instructions. In addition, it automatically generates simultaneous overlap of parallel operations (pipelining) to yield significant gains in effective processor execution speed. The two types

43

of pipelining include overlap of memory address calculations with memory access, and overlap of instructions permitted by separated function execution modules.

13.5.3 Implementation

The $3081/E$ processor hardware is incorporated into the Mark II online data acquisition system and the software is currently undergoing testing before implementation. The data flow between the VAX and $3081/E$ is controlled by two SSPs on a cable segment. The communication between the SSPs and the $3081/E$ processor is facilitated by an interface [37, 44] within the $3081/E$ chassis. The interface consists of two boards, one of which is specific to FASTBUS and the other a common interface board useable by other interfacing schemes. The FASTBUS board is a dual-ported slave, permitting access from either of two cable segments. This arrangement provides for loading new data into one processor while fetching processed output from another. The common interface board supports transfers at 25 Mbyte/sec to and from $3081/E$ memory and provides control of program execution.

13.5.4 Performance

The degree to which a particular application software permits pipelining can result in large performance variations. A version of the full Mark II event reconstruction analysis program has been successfully implemented on the $3081/E$. Preliminary performance tests used high-multiplicity Monte Carlo hadronic events at SLC energies. When the kernel of the program (the dominant user of CPU time) is translated with pipelining options, the processor takes about twice as long to process events as the SLAC IBM 3081K mainframe computer. When the pipelining is suppressed, the performance degrades by about 40%. Similar results have been achieved with a sample of PEP Bhabha scattering events.

14. SUMMARY

The properties of the various components of the detector are summarized in table 5. Most of the quoted resolutions were measured using Bhabha scattering events at PEP; the individual chapters should be consulted for more details.

15. ACKNOWLEDGMENTS

There are many people who have contributed to the design, construction and operation of the Mark II detector over the past 12 years. The fact that several components of the original detector built at SPEAR are in use today is a tribute to the skill of those involved. We gratefully acknowledge all of the physicists, engineers and technicians who have helped us over the years. We also wish to acknowledge the important contributions of the following people to the design and engineering studies leading to the successful upgrade of the Mark II detector: R. Baggs, D. Bernstein, L. Barker, K. Bouldin, H. Brafman, D. Briggs, R. Cooper, D. Day, B. Denton, S. Dyer, R. Fuzesy, B. Gray, J. Hanson, C. Hoard, D. Horelick, R. Horne, N. Hower, R. Jared, F. Kirsten, M. LaTeur, J. Mann, J. Mark, B. Martin, K. Mirk, T. Nakashima, W. Nilsson, J. Olsen, E. Ordinario, L. Paffrath, W. Pope, D. Porat, H. Rogers, W. Rowe, R. Stickley, M. Studzinski, Y.-Y. Sung, J. Tinsman, T. Walker, K. Warfield, and T. Webster.

REFERENCES

1. B. Richter, SLAC–PUB–4367, *1987 Lepton and Photon Symposium*. SLAC–229, *Conceptual SLC Design Report*, June 1980.

2. Mark II Collaboration, Proposal for the Mark II at the SLC, CALT–68–1015, April 1983 (also SLAC–PUB–3561, January 1985).

3. W. Farr *et al.*, *Nucl. Instr. and Meth.* **156** (1978) 283.

4. G. Hanson, *Nucl. Instr. and Meth.* **A252** (1983) 343.

5. D. Briggs *et al.*, *IEEE Trans. Nucl. Sci.* **NS–32** (1985) 653.

6. D. Bernstein *et al.*, *IEEE Trans. Nucl. Sci.* **NS–33** (1986) 86.

7. H. Brafman *et al.*, *IEEE Trans. Nucl. Sci.* **NS–32** (1985) 336.

8. J. Perl *et al.*, *Nucl. Instr. and Meth.* **A252** (1986) 616.

9. J. Va'Vra *et al.*, *Nucl. Instr. and Meth.* **203** (1982) 109.

10. D. Schaile *et al.*, *Nucl. Instr. and Meth.* **A242** (1986) 247.

11. Manufactured by Kyowa Gas Chemical Industry, Japan. T. Inagaki and R. Takashima, *Nucl. Instr. and Meth.* **201** (1982) 511.

12. Sylguard 184 resin and curing agent mixed with Dow Corning 200 Electronic Fluid with the viscosity of 20 cent. stokes.

13. J. E. Grund, *IEEE Trans. Nucl. Sci.* **NS–27** (1980) 599. J. S. Brown *et al.*, *Nucl. Instr. and Meth.* **221** (1984) 503.

14. M. Breidenbach *et al.*, *IEEE Trans. Nucl. Sci.* **NS–25** (1978) 706.

15. W. Braunschweig *et al.*, *Nucl. Instr. and Meth.* **134** (1976) 261.

16. G. S. Abrams *et al.*, *IEEE Trans. Nucl. Sci.* **NS–25** (1978) 309. G. S. Abrams *et al.*, *IEEE Trans. Nucl. Sci.* **NS–27** (1980) 59.

17. W. J. Willis and V. Radeka, *Nucl. Instr. and Meth.* **120** (1974) 221.

18. E. Cisneros *et al.*, *IEEE Trans. Nucl. Sci.* **NS–24** (1977) 413.

19. R. L. Ford and W. R. Nelson, EGS3, SLAC–210, June 1978.

20. M. Nelson *et al.*, *Phys. Rev. Lett.* **50** (1983) 1542.

21. M. E. Nelson, Ph.D. thesis, LBL–16724mc, October 1983.
    D. A. Karlen, Ph.D. thesis, SLAC–325, March 1988.

22. J. A. Kadyk, *Proceedings of the Gas Sampling Calorimetry Workshop II*, Batavia, IL (1985) 373.

23. R. C. Jared *et al.*, *IEEE Trans. Nucl. Sci.* **NS–33** (1986) 916.

24. Manufactured by BICRON Corporation, Newbury, OH.

25. W. R. Nelson *et al.*, SLAC–Report–265, December 1985.

26. E. Cisneros *et al.*, *IEEE Trans. Nucl. Sci.* **NS–28** (1981) 465.

27. H. Brafman *et al.*, SLAC–PUB–2033, October 1977.
    T. Himel, Ph.D. thesis, SLAC–REP–223, October 1979.

28. J. E. Grund, *IEEE Trans. Nucl. Sci.* **NS–26** (1979) 220.

29. R. Aleksan *et al.*, *Proceedings of the International Conference on The Impact of Digital Microelectronics and Microprocessors on Particle Physics, World Scientific* (1988) 38.

30. Mark II Collaboration and SLC Final Focus Group, SLAC–SLC–PROP–2, April 1986.

31. M. Levi *et al.*, *Precision Measurements of the SLC Spectrometer Magnets*, SLAC–PUB–4654.

32. There are different definitions of critical energy that are commonly used. This paper uses J. D. Jackson, *Classical Electrodynamics*, 2nd edition, John Wiley and Sons (1975) 675.

33. Iron-nickel alloy with low thermal expansion coefficient.

34. J. Seeman *et al.*, SLAC–PUB–3945, April 1986, published in proceedings LINAC86, 441.

35. D. J. Nelson *et al., IEEE Trans. Nucl. Sci.* **NS–28** (1981) 336.

36. E. J. Siskind, *IEEE Trans. Nucl. Sci.* **NS–30** (1983) 188.

37. A. J. Lankford and T. Glanzman, *IEEE Trans. Nucl. Sci.* **NS–31** (1984) 225.
    T. Barklow *et al., IEEE Trans. Nucl. Sci.* **NS–33** (1986) 775.

38. J. T. Walker *et al., Nucl. Instr. and Meth.* **226** (1984) 200.
    G. Anzivino *et al., Nucl. Instr. and Meth.* **A243** (1986) 153.

39. C. Adolphsen *et al., IEEE Trans. Nucl. Sci.* **NS–33** (1986) 57.
    C. Adolphsen *et al., Nucl. Instr. and Meth.* **A253** (1987) 444.
    C. Adolphsen *et al., IEEE Trans. Nucl. Sci.* **NS–35** (1988) 424.

40. K. Hayes, *Nucl. Instr. and Meth.* **A265** (1988) 60.
    J. Jaros in Vertex Detectors, F. Villa, ed., Plenum Press, New York (1988) 37.

41. L. Barker, SLAC–PUB–4757, October 1988.

42. J. Alexander *et al., Nucl. Instr. and Meth.* **A252** (1986) 60.

43. P. Rankin *et al., Proceedings of the Conference on Real-Time Computer Applications in Nuclear and Particle Physics,* Chicago, Illinois (1985) 1321.
    P. F. Kunz *et al., Proceedings of the Symposium on Recent Developments in Computing, Processor, and Software Research for High-Energy Physics,* Guanajuato, Mexico (1984) 197.
    P. F. Kunz *et al., Proceedings of the Three-Day In-Depth Review on the Impact of Specialized Processors in Elementary Particle Physics,* Padova, Italy (1983) 84.

44. L. Barker *et al., Proceedings of the Nuclear Science Symposium,* San Francisco, California (1985) 793.

FIGURE CAPTIONS

1) Cut-away view of the upgraded Mark II detector showing major components. The two vertex detectors are not currently installed.

2) Cell design for the central drift chamber.

3) Schematic of the central drift chamber electronics.

4) Tracking efficiency for the central drift chamber as a function of $\cos\theta$. The hadronic events (boxes) are from a Monte Carlo study at SLC energies; the Bhabha scattering events (dots) are from a sample of PEP data. Error bars are shown only for the Monte Carlo events.

5) Central drift chamber position resolution versus drift distance, with (solid circles) and without (open circles) the time-slewing correction.

6) Efficiency for separating two tracks as a function of their distance apart for the central drift chamber TDCs (X's) and FADCs (closed circles).

7) Momentum resolution for the central drift chamber. The tracks are selected from Bhabha scattering events and a constraint that the track originate from a single point is used. The magnetic field was 4.5 kG.

8) dE/dx versus momentum as measured for tracks at PEP. The number of particles in the electron, muon, kaon and proton bands are enhanced relative to the pion band that would normally dominate the plot.

9) Electron-pion separation for tracks in the momentum range 0.25–0.60 GeV/c. The particles are from two different event samples and so are not in their usual proportions.

10) Laser calibration system schematic for the TOF system. The figure also shows the locations for the calibration optical fibers in a typical counter.

11) Resolution of TOF system obtained from a sample of Bhabha events.

12) Pion/kaon/proton separation using the TOF system. Data are from PEP.

13) Electron-hadron separation for dE/dx without (solid line) and with (dashed line) TOF information. The dips in the solid line occur when the noted particle and the electron have the same dE/dx value for the same momentum (see fig. 8).

14) Ganging scheme for the channels in the liquid argon barrel calorimeter.

15) Measured energy distribution for the liquid argon calorimeter from Bhabha scattering events at PEP. The histogram represents Monte Carlo simulation.

16) Monte Carlo simulation of the barrel calorimeter energy resolution as a function of energy and angle of incidence. The three values shown for angle of incidence are 8.1° (open circles), 25.0° (closed circles), and 35.7° (boxes).

17) Total calorimeter thickness (solid line) and number of sampling layers (dashed line) vs. $\cos\theta$. The shaded area shows the region used for calculating the solid angle coverage.

18) Response of the endcap calorimeter to small numbers (1-5) of 10-GeV positrons.

19) Cross section of a muon module.

20) Side view of one of the four SAM modules showing its location inside the Mark II detector.

21) View of two SAM modules as seen from the interaction point. The figure shows the orientation of drift and proportional tubes as well as the method of assembly around the beam pipe.

22) Small-angle coverage in the Mark II.

23) Geometry of the Mini-SAM. As an example, in the 'Signal Used' definition, 12S means the signal sum of quadrants 1 and 2 being over a Bhabha threshold in the south monitor.

24) Block diagram of the charged particle trigger.

25) Conceptual design of the Extraction Line Spectrometer (ELS) system.

26) Cross section of a B32 magnet showing the locations of magnetic strength measuring devices in the magnet gap.

27) Schematic view of the Phosphorescent Screen Monitor (PSM).

28) FASTBUS architecture for the Mark II data acquisition system.

29) The layout of the Silicon Strip Vertex Detector (SSVD).

30) The plan for a silicon detector module. All dimensions are in mm.

31) Cut-away drawing of the Drift Chamber Vertex Detector (DCVD).

32) Wire and electrode placement in the jet cells of the DCVD.

33) Schematic drawing of lower muon facade.

34) Schematic view of the Wire Imaging Synchrotron Radiation Detector (WISRD).

Table 1.   Design parameters for the central drift chamber.

Layer	Radius at Center (cm)	Stereo Angle (Degrees) Wire 1	Wire 6	Number of Cells
1	27.05	0	0	26
2	38.25	3.65	4.07	36
3	48.45	0	0	46
4	59.25	−3.73	−4.00	56
5	69.45	0	0	66
6	80.15	3.76	3.96	76
7	90.35	0	0	86
8	100.95	−3.77	−3.93	96
9	111.15	0	0	106
10	121.65	3.77	3.91	116
11	131.85	0	0	126
12	142.35	−3.78	−3.89	136

Table 2.   Orientation, width and number of strips per layer in each liquid argon module.

Strip Layer	Coordinate Measured	Number of Strips	Strip Width (cm)
Trigger	ϕ	36	3.5
1	ϕ	38	3.5
2	θ	100	3.5
3	U	70	5.4
4	ϕ	38	3.5
5	θ	100	3.5
6	U	70	5.4
7	ϕ	40	3.5
8	θ	100	3.5
9	U	70	5.4
10	ϕ	40	3.5
11	θ	100	3.5
12	θ	100	3.5
13	θ	100	3.5
14	ϕ	40	3.5
15	ϕ	40	3.5
16	ϕ	40	3.5
17	ϕ	40	3.5
18	ϕ	40	3.5

Table 3.   Muon absorber geometry: d is the perpendicular distance of the absorber from the interaction point; λ is the thickness of the absorber in nuclear interaction lengths.

	East		Top		West		Bottom	
Level	d (m)	λ	d (m)	λ	d (m)	λ	d (m)	λ
Before 1		1.17		1.17		1.17		1.17
1	3.2	1.38	2.5	1.38	3.2	1.38	2.5	1.38
2	3.6	1.40	2.8	1.40	3.6	1.40	2.8	1.40
3	4.0	1.85	3.2	1.81	4.0	1.85	3.2	1.85
4	4.5	1.49	3.6	1.40	4.5	1.49	3.6	1.85
Total		7.28		7.16		7.28		7.65

Table 4.   *Properties of the Silicon Strip Vertex Detector.*

Detector Property	Layer 1	Layer 2	Layer 3	Units
Layer radius	28	33	37	mm
Strip pitch	25	29	33	μm
Strip width	8	8	8	μm
Active length	72	82	90	mm
Depletion voltage	~ 55	~ 55	~ 55	V
Capacitance* (to other strips)	8.2	8.8	9.3	pF
Capacitance* (to backplane)	0.6	0.8	1.0	pF

* Calculated.

Table 5.   *Summary of detector properties.*

Central Drift Chamber	• Active length 2.30 m.
	• Inner radius 0.192 m, outer radius 1.52 m.
	• Six axial layers, six stereo layers.
	• Jet-chamber cell with six sense wires.
	• 89% Ar, 10% CO_2, 1% CH_4.
	• Position resolution 170 μm.
	• Momentum resolution $\sigma(p)/p^2 = 0.31\%$ $(GeV/c)^{-1}$.
	• dE/dx resolution 7.2% for minimum ionizing particles.
Time-of-Flight	• 48 scintillation counters read out at both ends.
	• Inner radius 1.52 m, covers 70% of 4π.
	• $\sigma = 221$ ps.
	• e/π separation up to momenta of 10 GeV at 2σ level (combined with dE/dx).
Magnet	• 5.0 kG Al coil solenoid.
	• 1.56 m inner radius.
Electromagnetic Calorimetry	Barrel
	• Eight modules of Pb/liquid argon in an octagon around the coil.
	• 14.1 X_0, covers 64% of 4π.
	• 2-mm Pb sheets separated by 3-mm liquid argon gaps.
	• Strip readout in θ, ϕ, U directions.
	• $\Delta E/E = 13.3\%/\sqrt{E} \oplus 3.3\%$.
	Endcaps
	• Two annular Pb/proportional tube modules.
	• Inner radius 0.40 m, outer radius 1.46 m.
	• 18 X_0, 22% of 4π.
	— with the barrel, get full coverage for 86% of 4π.
	• 0.28-cm Pb sheets with 0.9 × 1.5 cm tubes.
	• 89% Ar, 10% CO_2, 1% CH_4.
	• Ganged readout in X, Y, U, V directions.
	• $\Delta E/E \cong 22\%/\sqrt{E}$.

Continued...

Muon System	• Proportional tubes interleaved with steel absorber (4 layers for 1.2-m total thickness). • Covers 45% of 4π.
Luminosity Monitors	Small Angle Monitor (SAM) • Covers 50 to ~160 mrad, 1.38 m in z from IP. • Nine layers of drift tubes for tracking. • Position resolution 250 μm. • 89% Ar, 10% CO_2, 1% CH_4. • Readout in Y, U, V directions. • Six layers of Pb/proportional tubes for calorimetry, 14.3 X_0. • $\Delta E/E = 45\%/\sqrt{E}$. Mini-SAM • Covers 15–25 mrad, 2.05 m in z from IP. • Six layers of tungsten/scintillator, 15 X_0. • $\Delta E/E = 35\%/\sqrt{E}$.
Small Electromagnetic Shower Detectors	Catcher/Mask Plug • 25–40 mrad, 1.02 m in z from IP. • Two layers of tungsten/scintillator. Active Mask • 30–50 mrad, .635 m in z from IP. • Three layers of lead/optical fiber. Endcap Veto Counter • 150–250 mrad, 1.9 m in z from IP. • Four layers of lead/scintillator. Liquid Argon Hole Taggers • 1.65 m long, inner radius 2.4 m. • Cover the $3°$ regions at junctions of liquid argon barrel calorimeter modules. • 2.5-cm-thick scintillator with 1.9 cm of lead preradiator.

MARK II AT SLC

Muon Chambers

Hadron Absorber

Muon Chambers

Solenoid Coil

Lead/Proportional
Tube Electromagnetic
Calorimeter

Mini-Small Angle
Monitor

Small Angle
Monitor

Silicon Strip
Vertex Detector

Drift Chamber
Vertex Detector

Central Drift
Chamber

Time-of-Flight
counter

Lead/Liquid Argon
Electromagnetic
Calorimeter
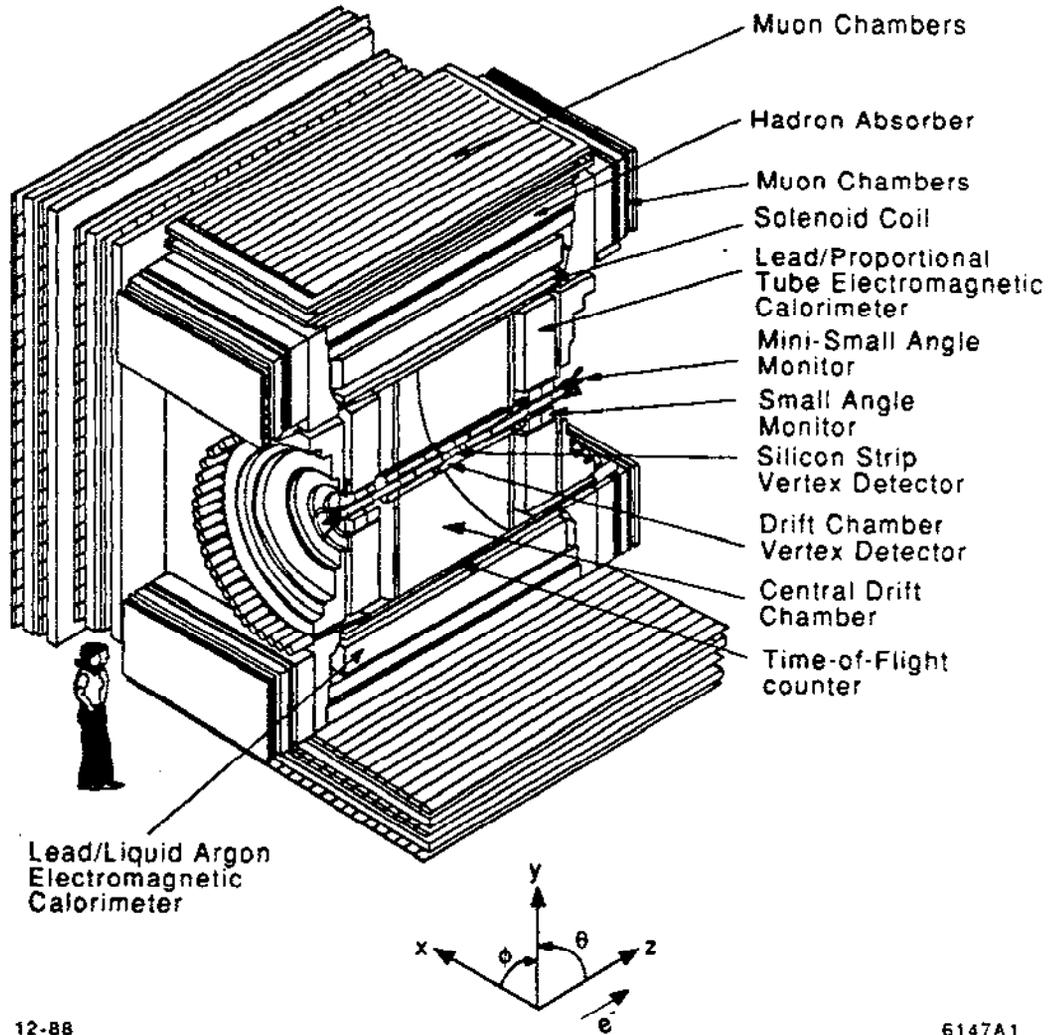
12-88

6147A1

Fig. 1

DRIFT CHAMBER WIRE PATTERN
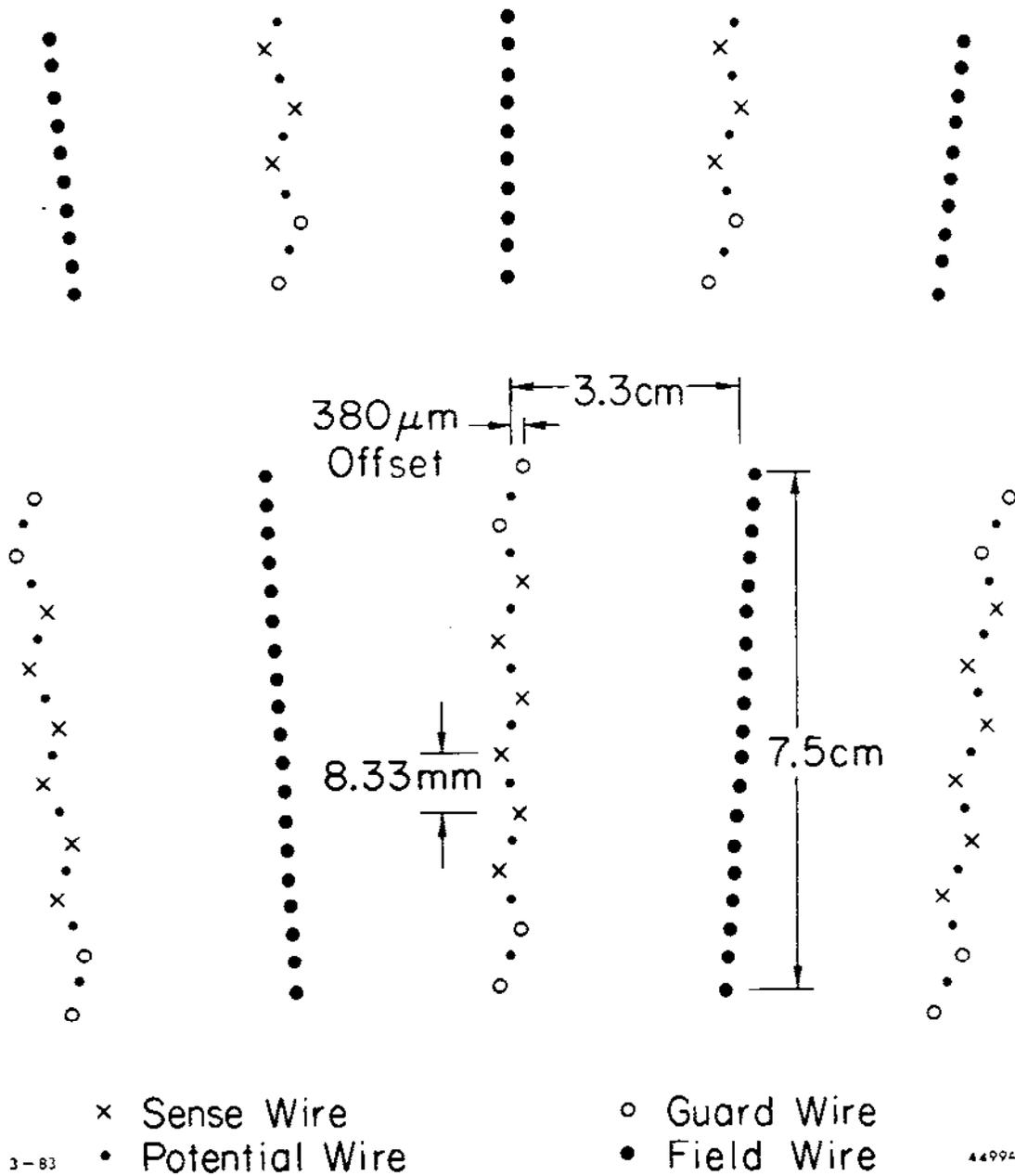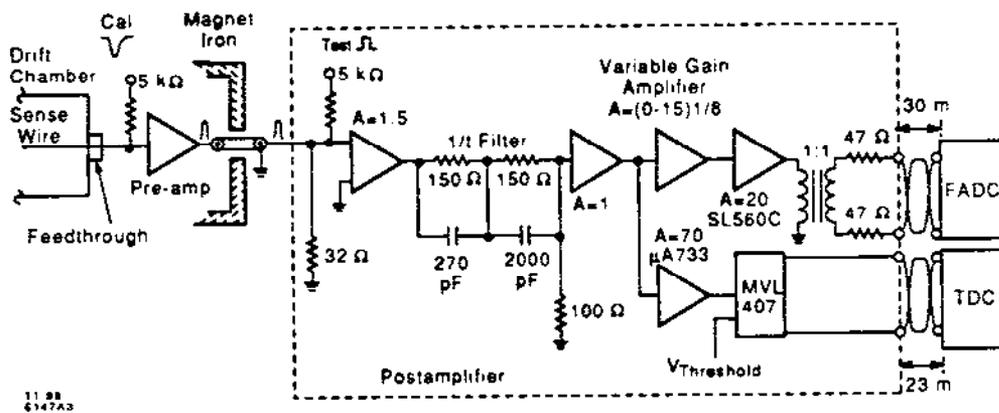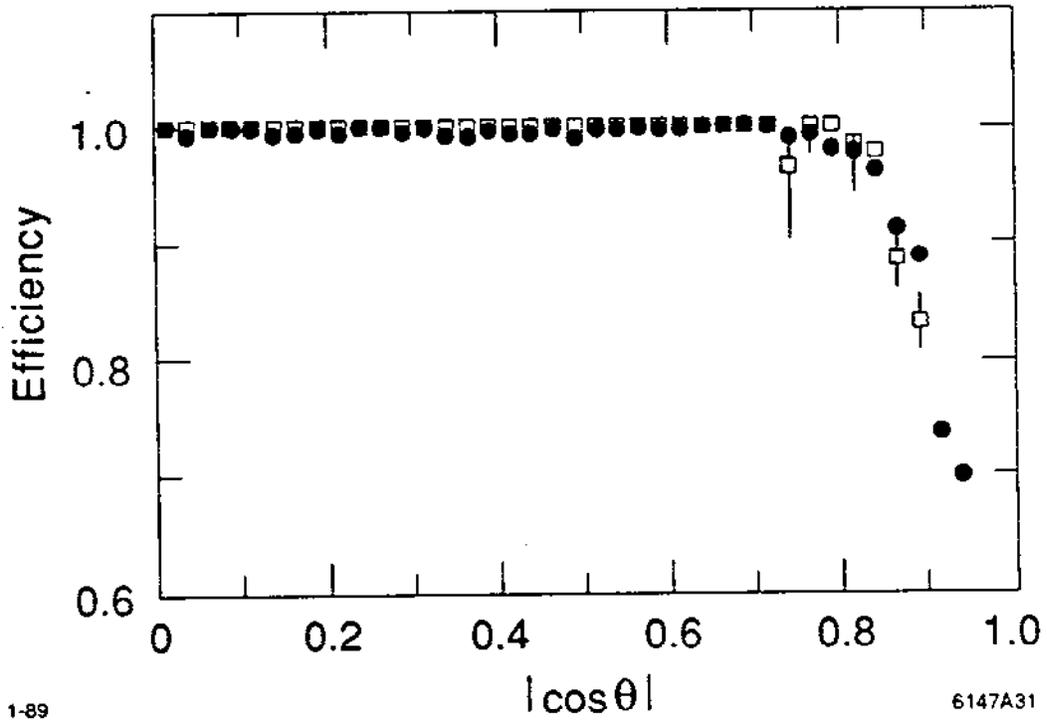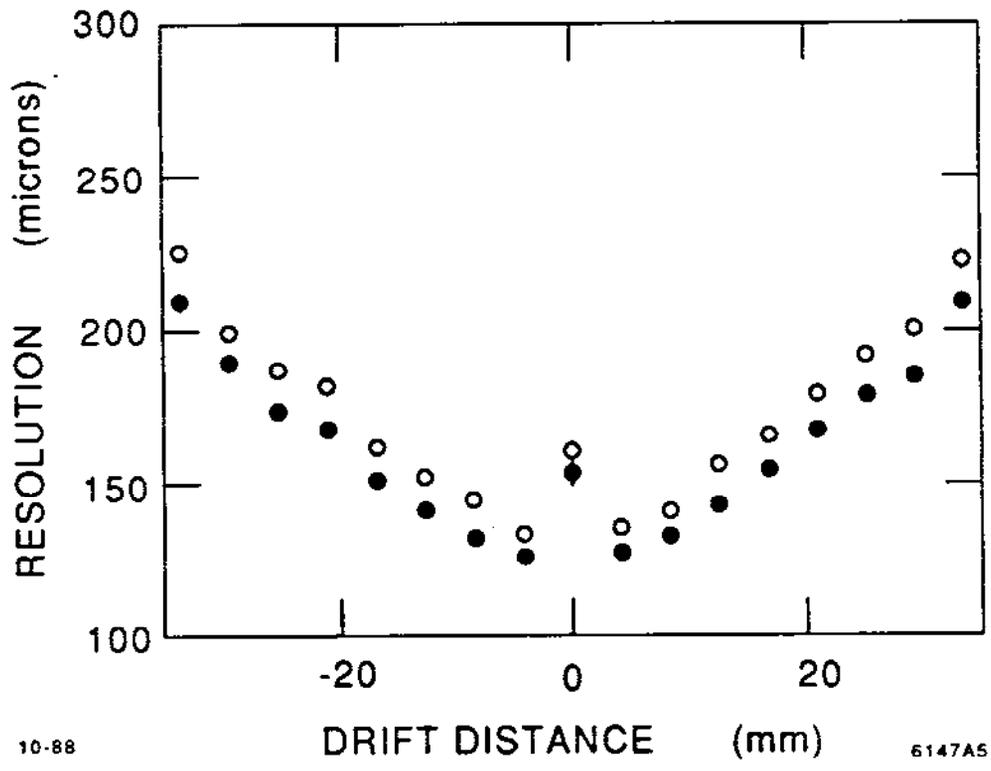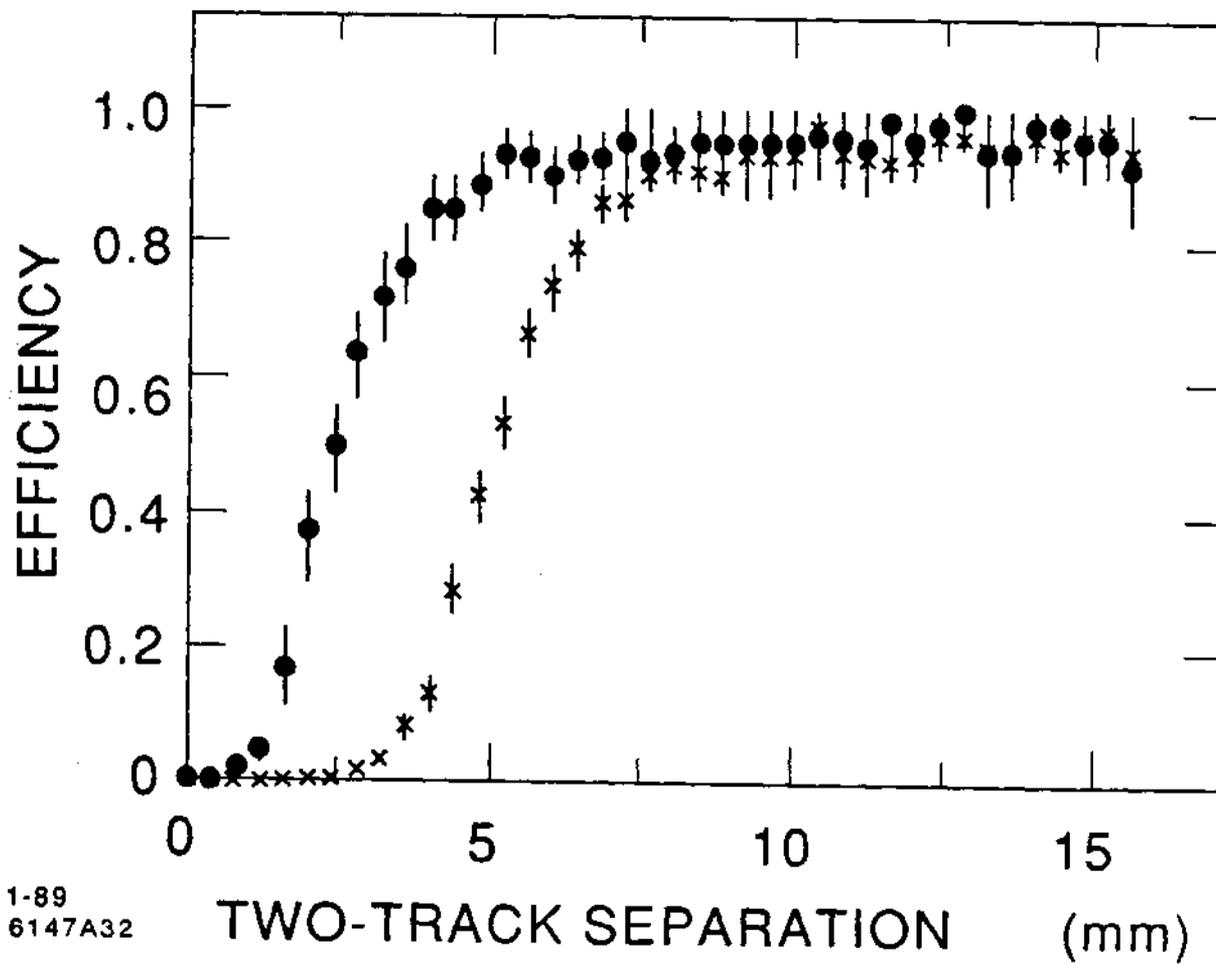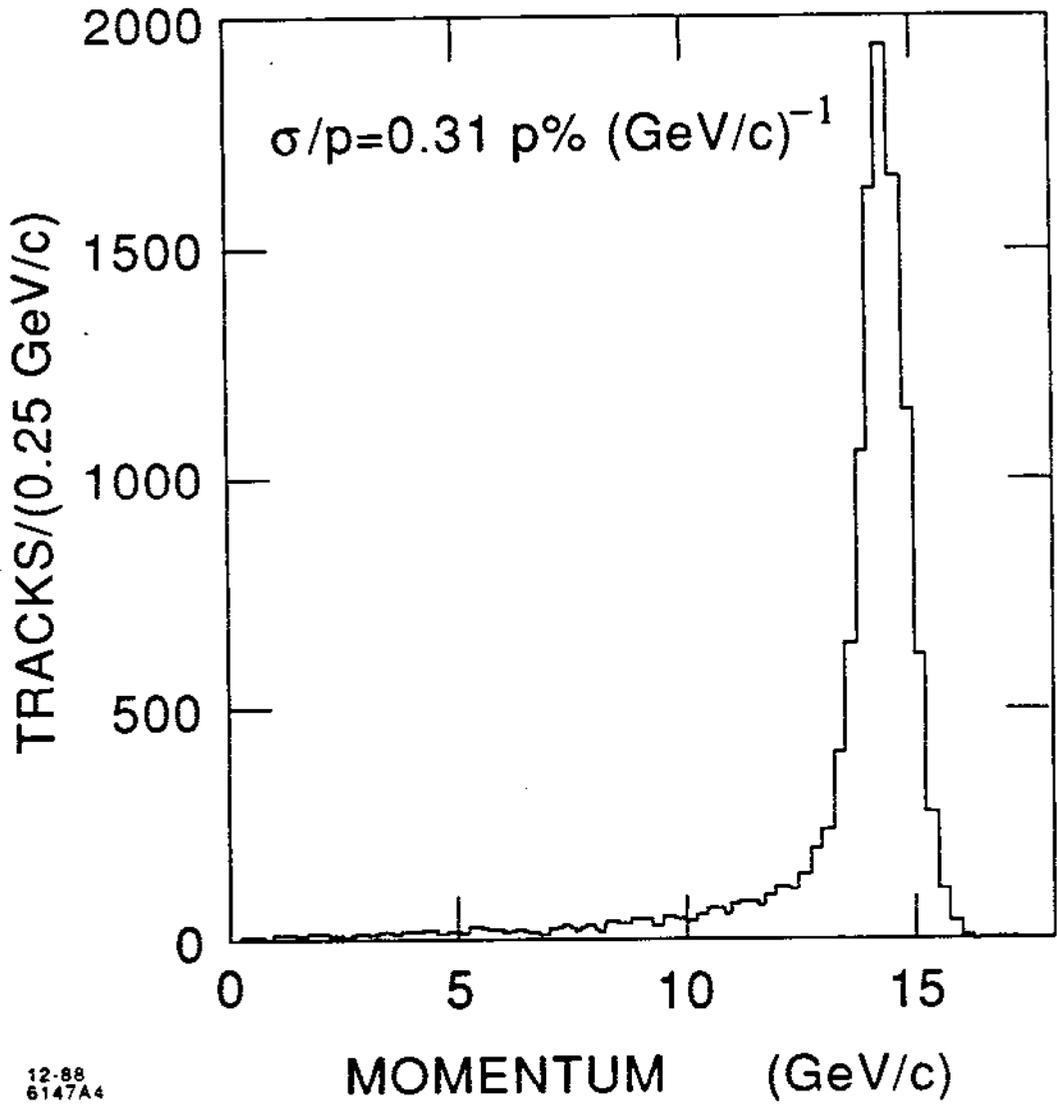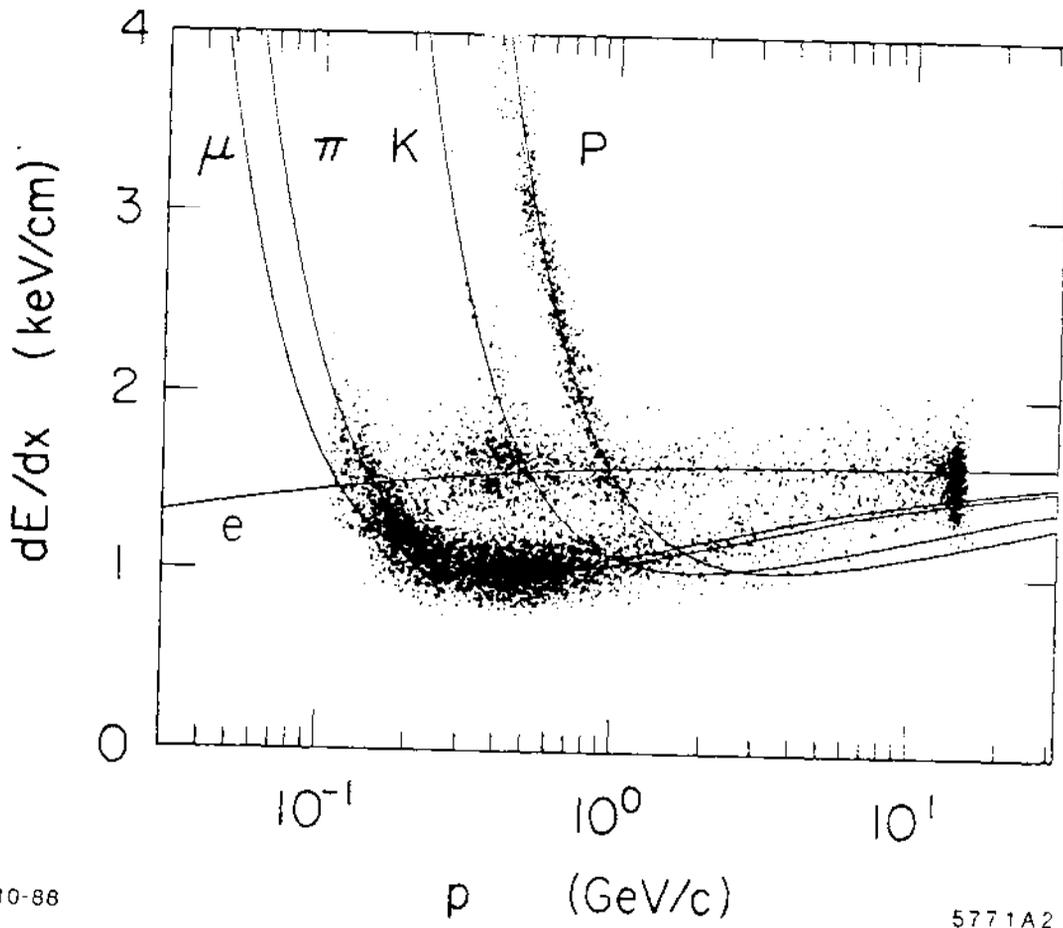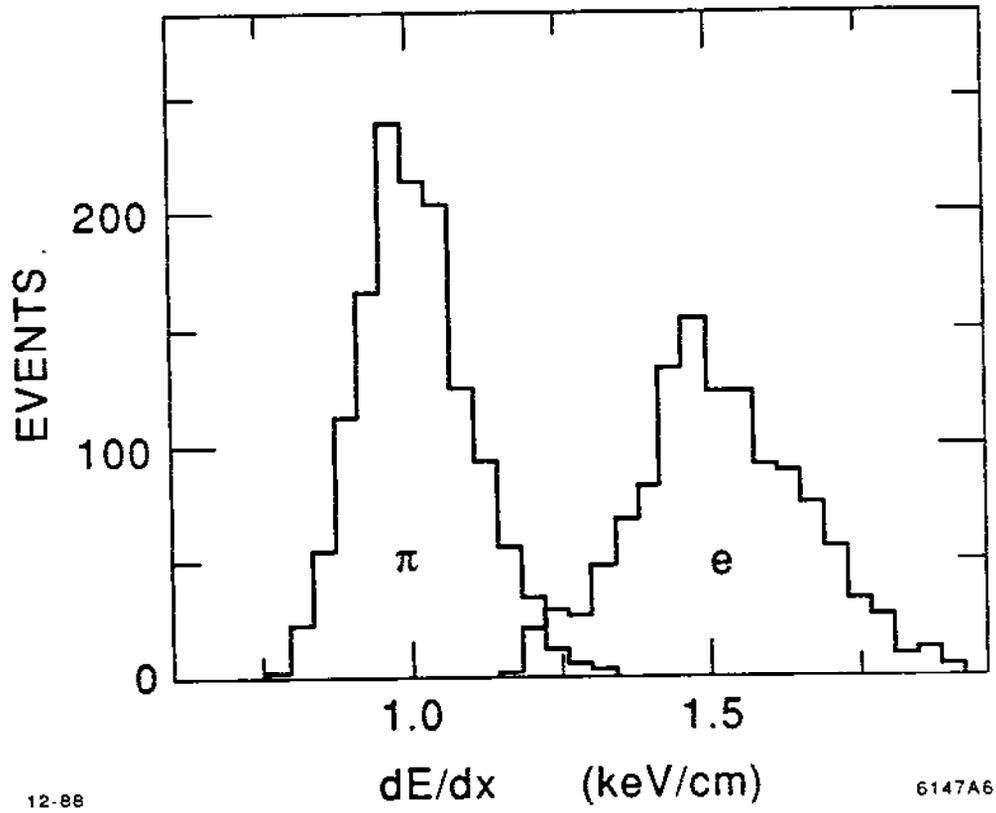
380 μm Offset

3.3cm

8.33mm

7.5cm

× Sense Wire
• Potential Wire
○ Guard Wire
• Field Wire

3–83

44994

Fig. 2

Fig. 3

Efficiency vs |cos θ|

Fig. 4

Fig. 5

Fig. 6

$\sigma/p = 0.31\ p\%\ (GeV/c)^{-1}$

Fig. 7

Fig. 8

EVENTS

200

100

0

π

e

1.0

1.5

dE/dx   (keV/cm)

12-88

6147A6

Fig. 9

Fig. 10

σ =221 ps

t measured - t predicted (ns)

10-88
6147A8

Fig. 11

Fig. 12

Fig. 13

F3

T2

F2

U

T1

F1

Massless Gap

10-88
6147A11

Fig. 14

Fig. 15

Fig. 16

1-89
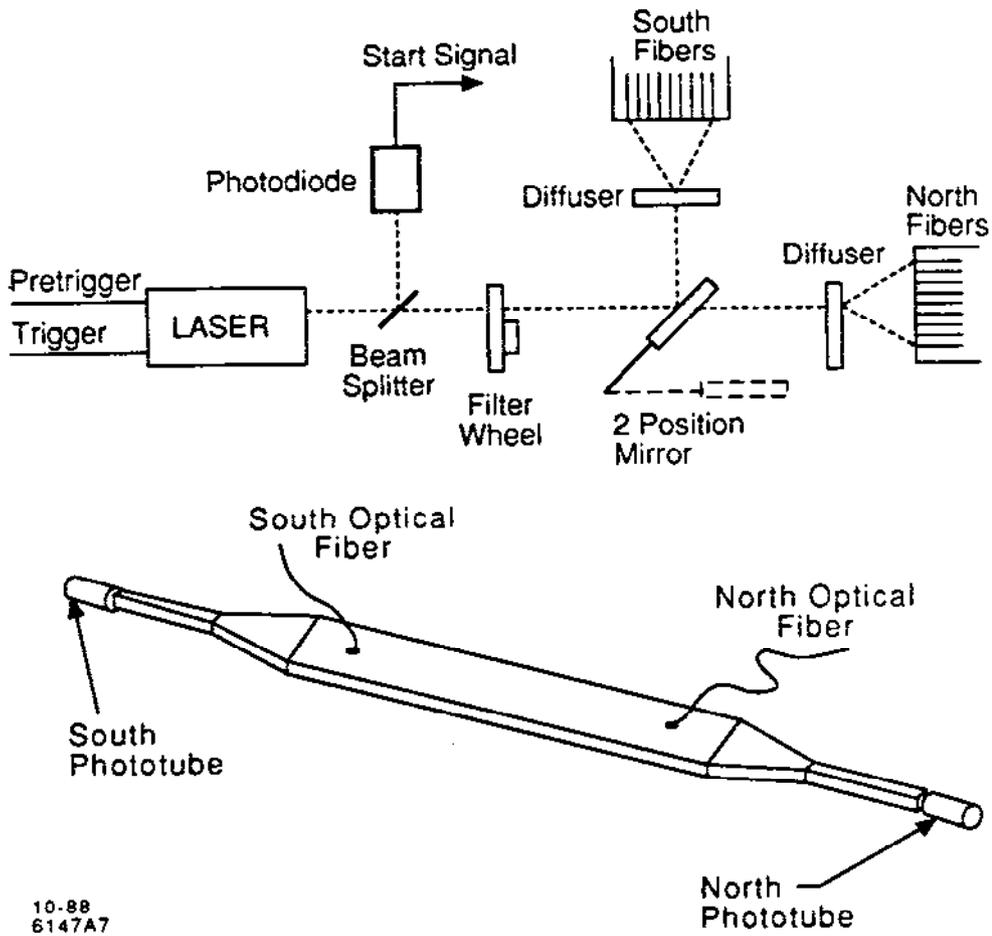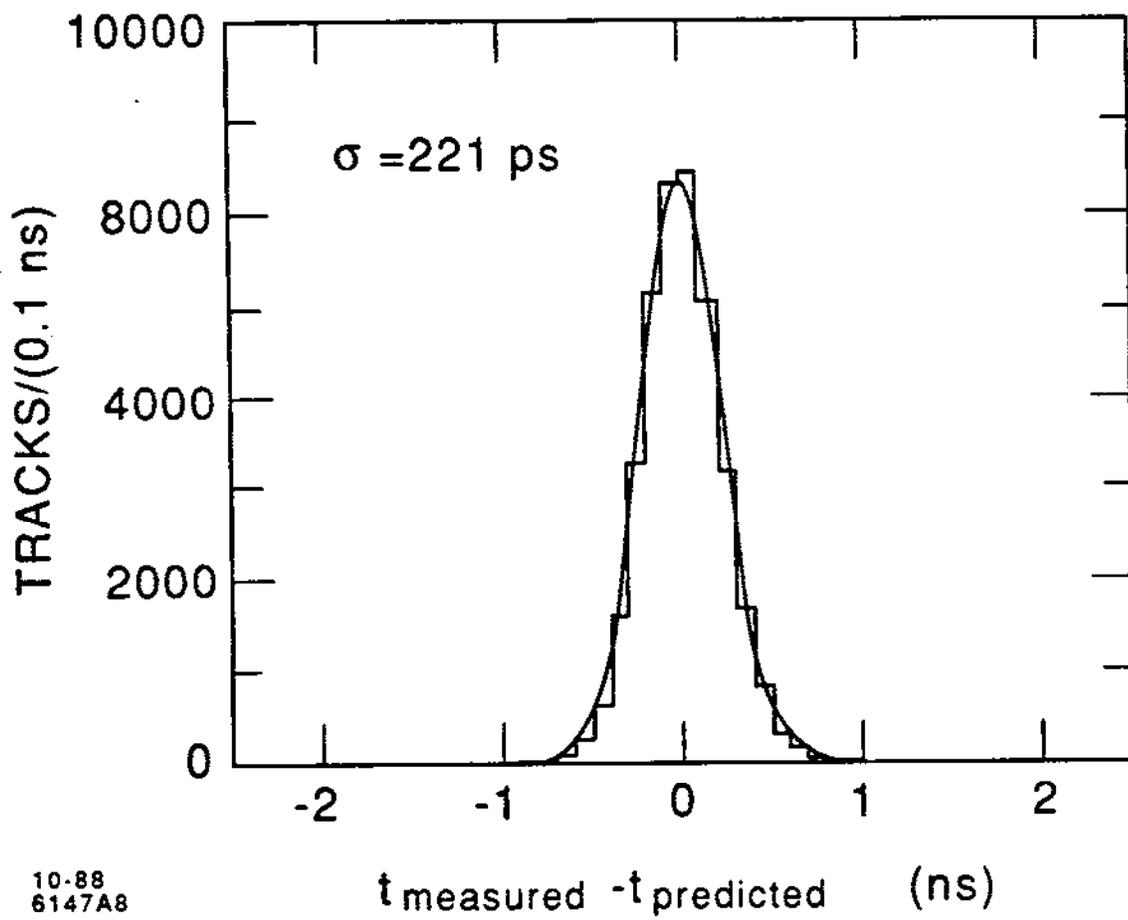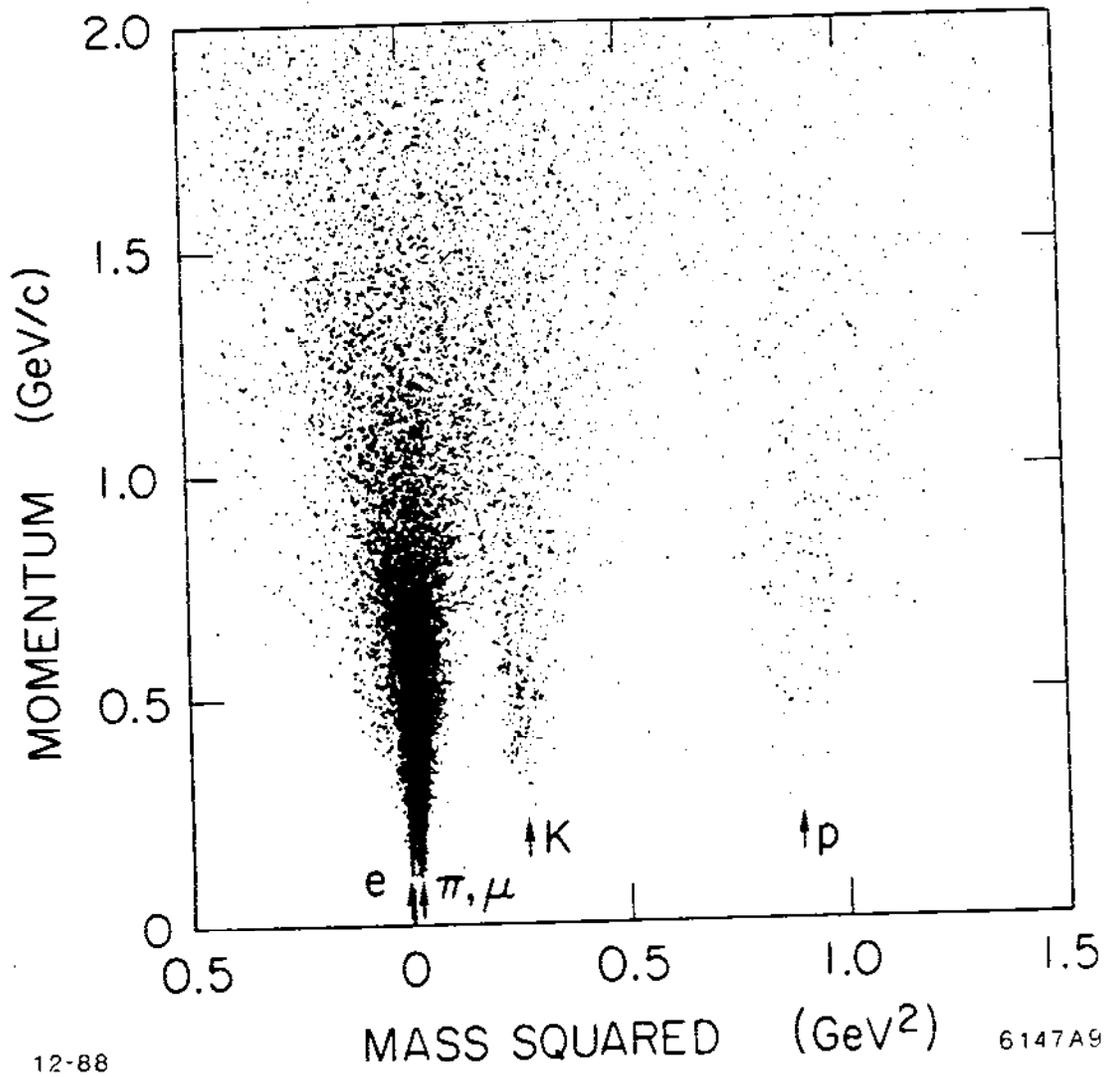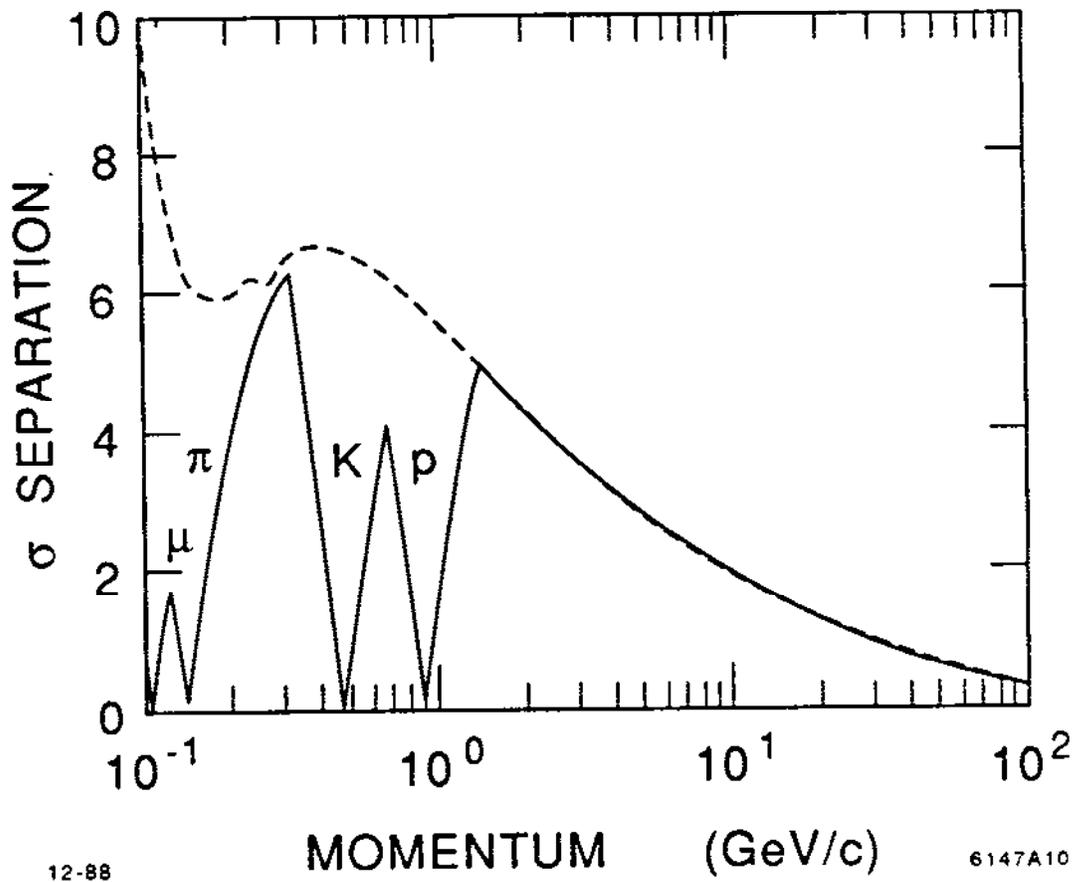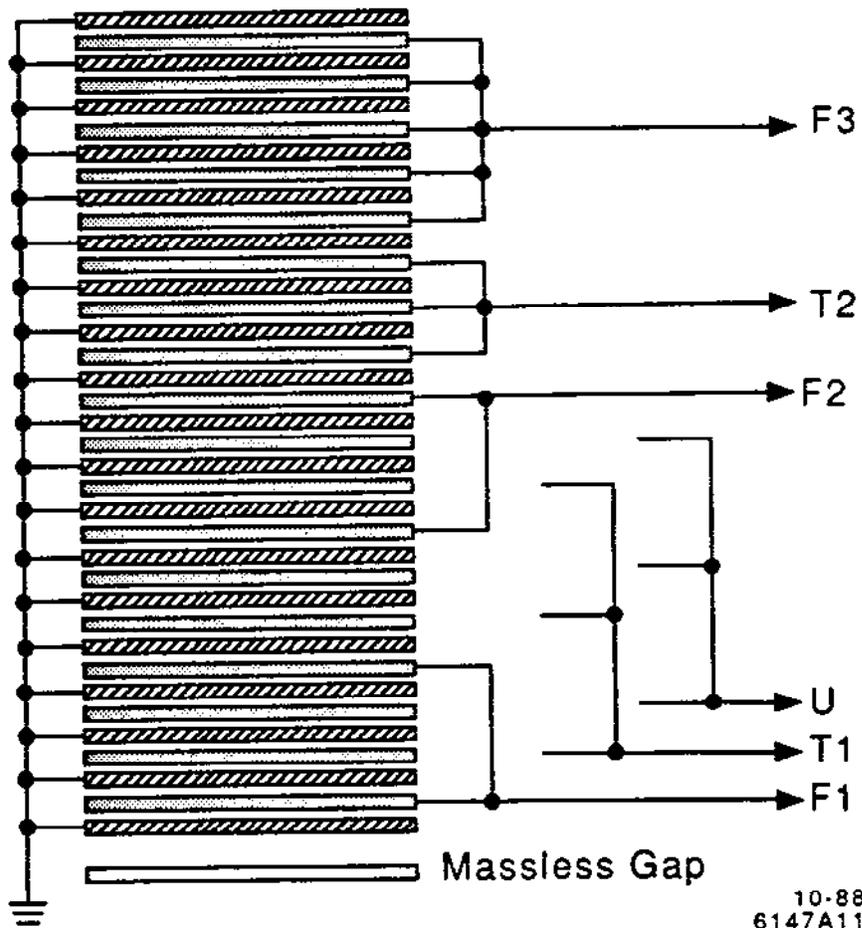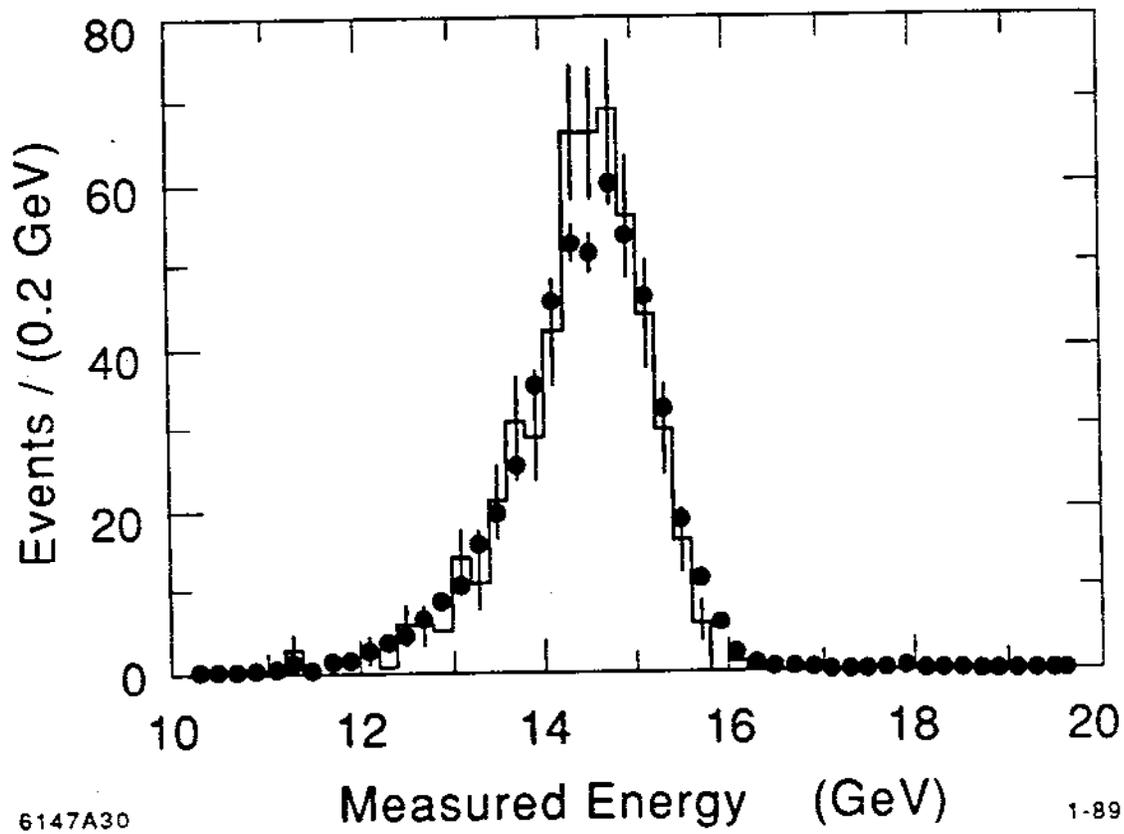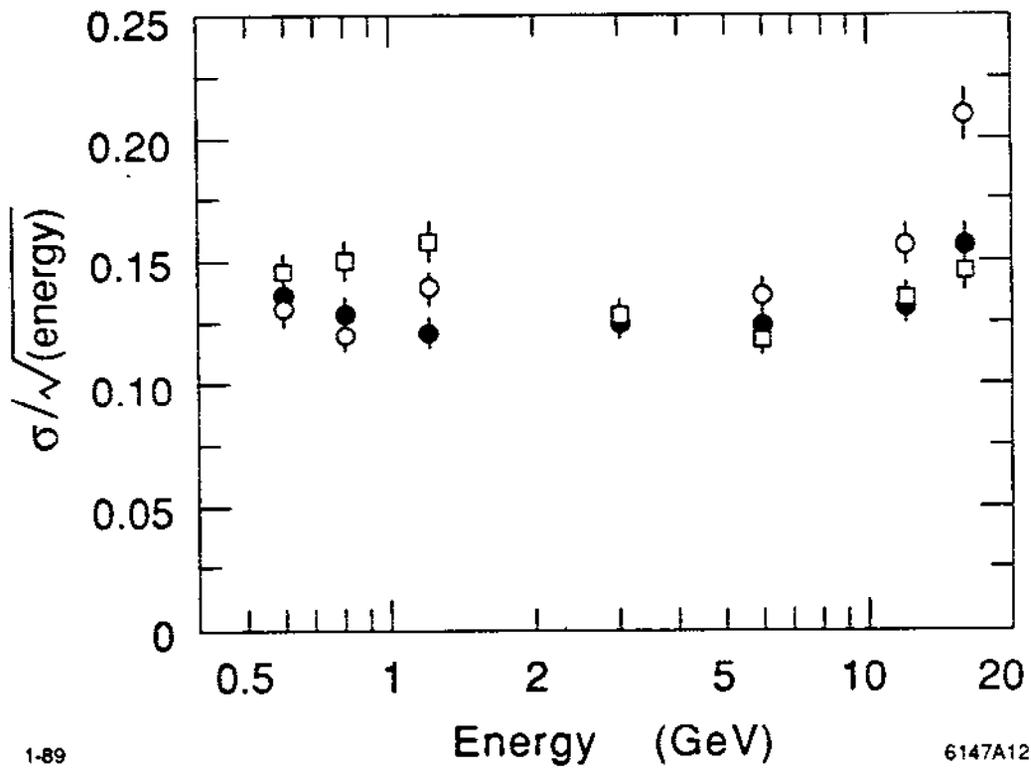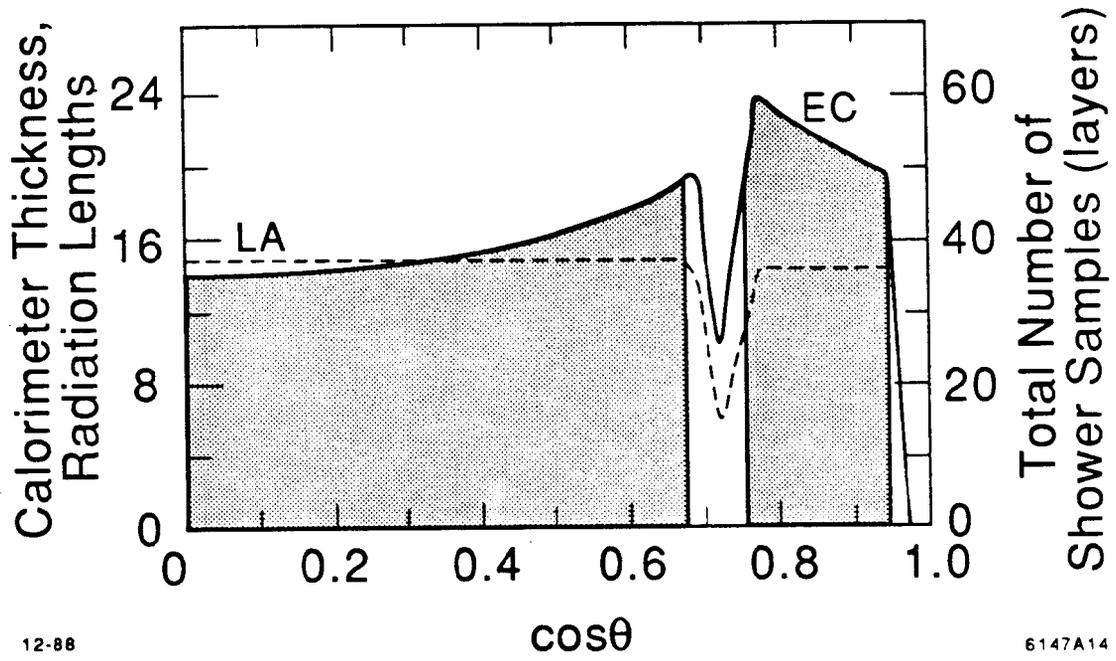
6147A12

Fig 17
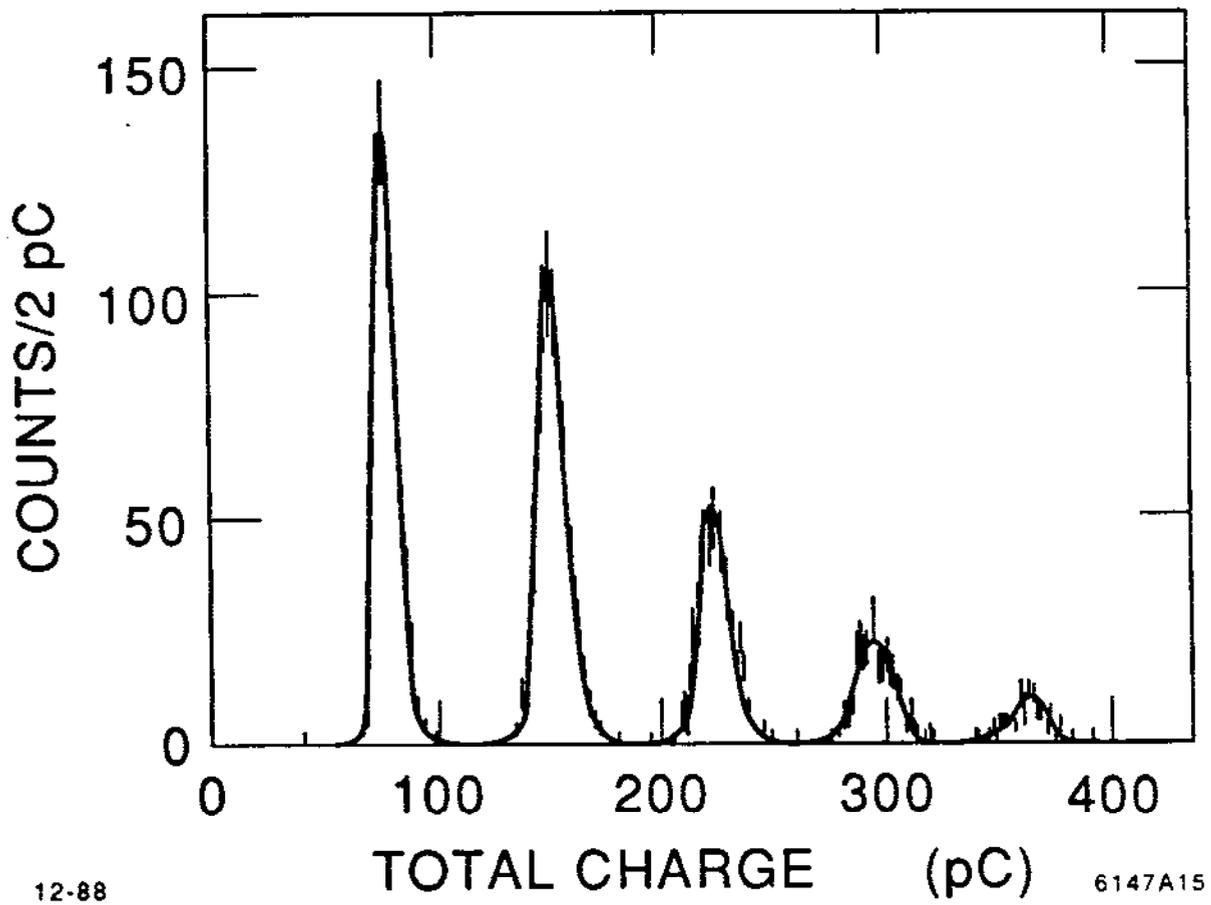
Fig. 18
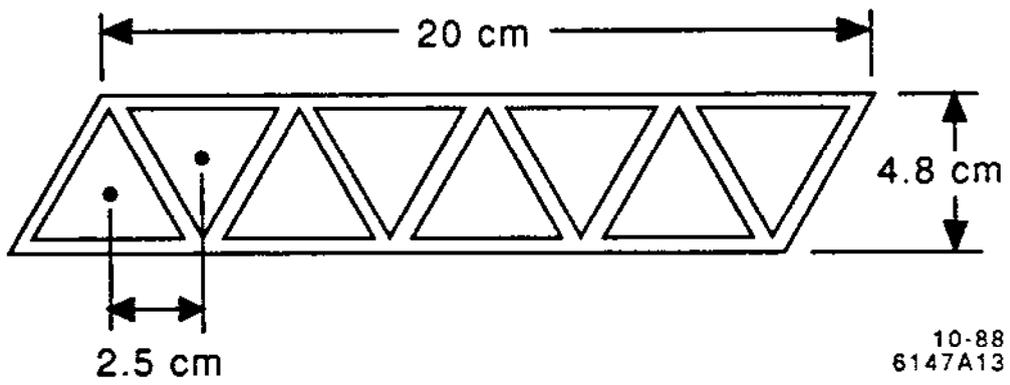
Fig. 19
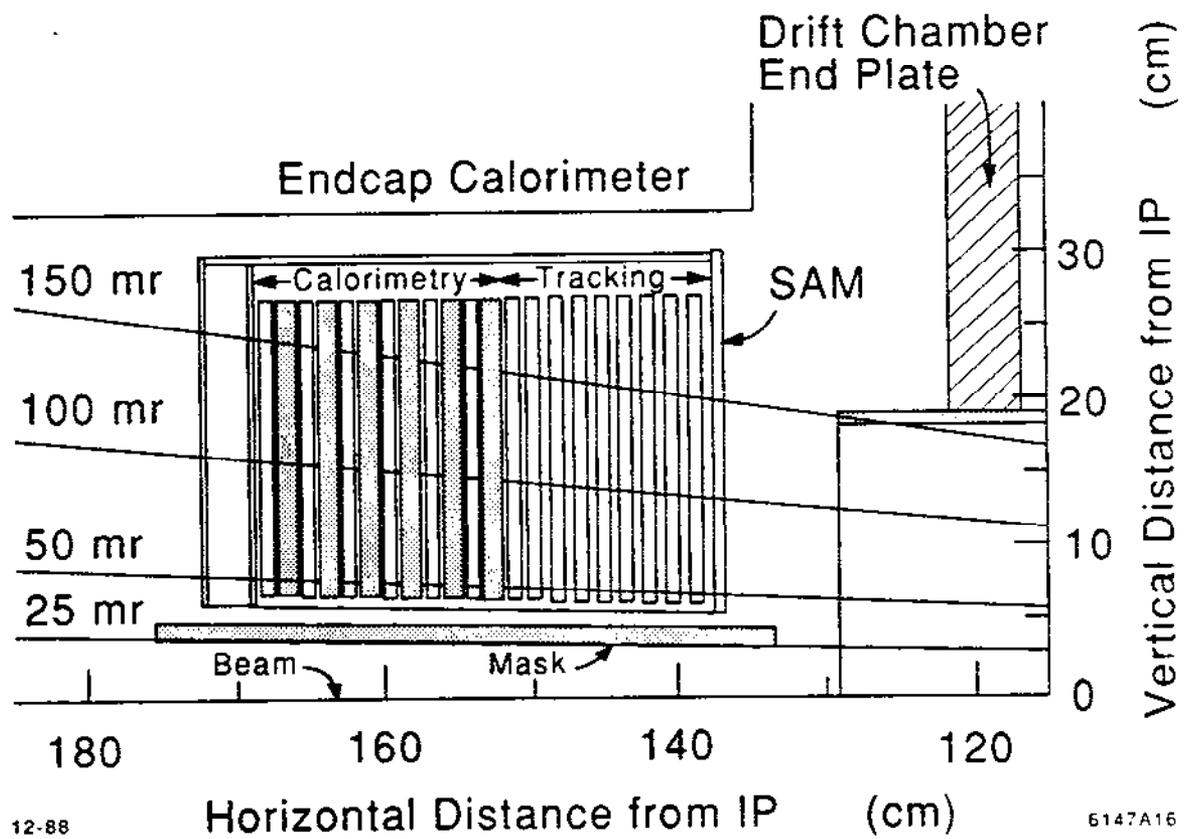
Fig. 20
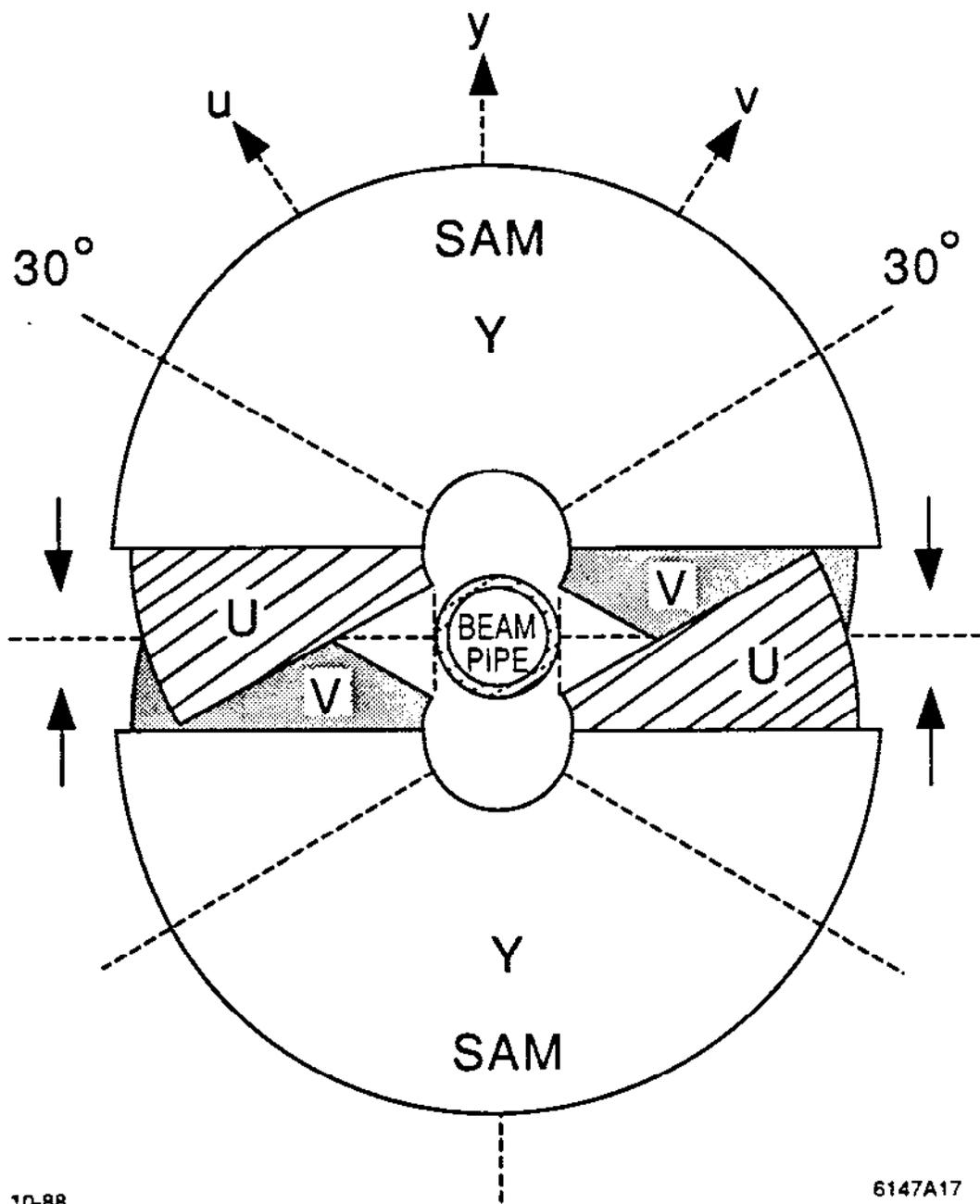
Fig. 21
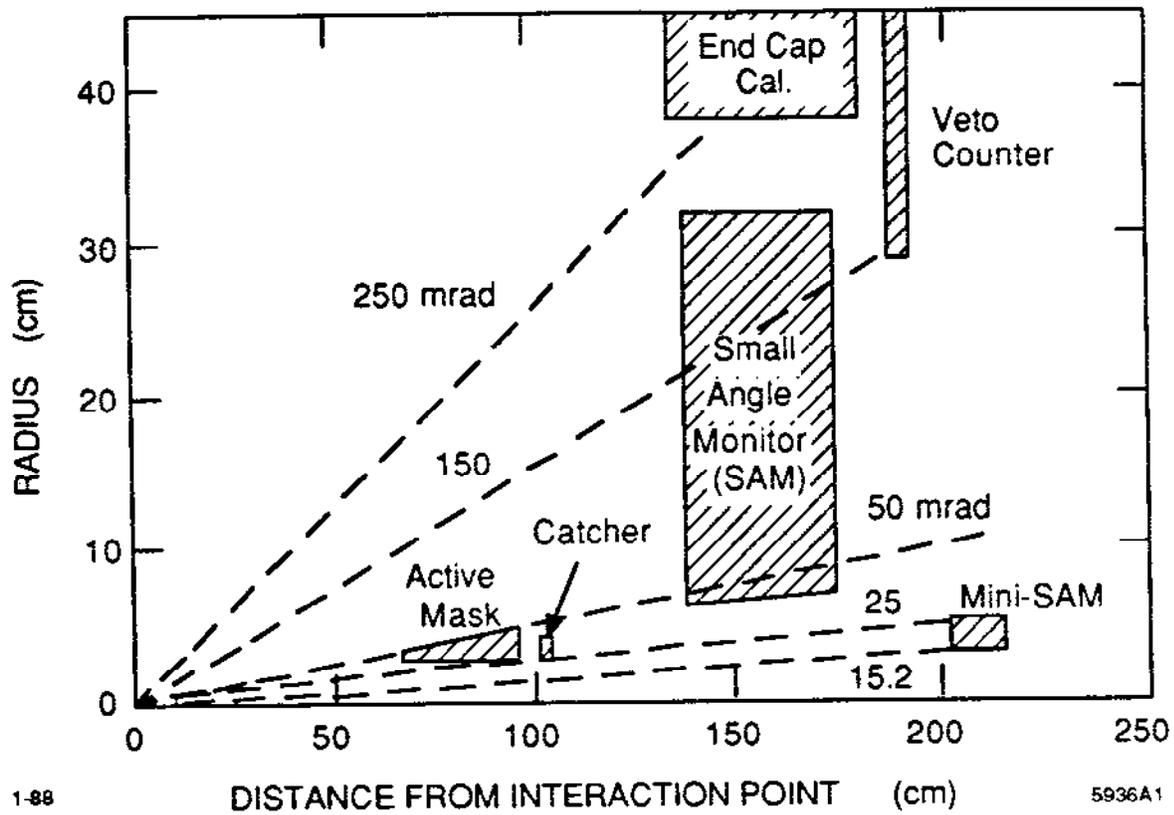
6147A17

Fig. 22

Signal used:
12S • 23N or 23S • 12N
or 34S • 14N or 14S • 34N

e^- e^+

S
1
4
2
3

N
1
2
4
3

← 205 cm →
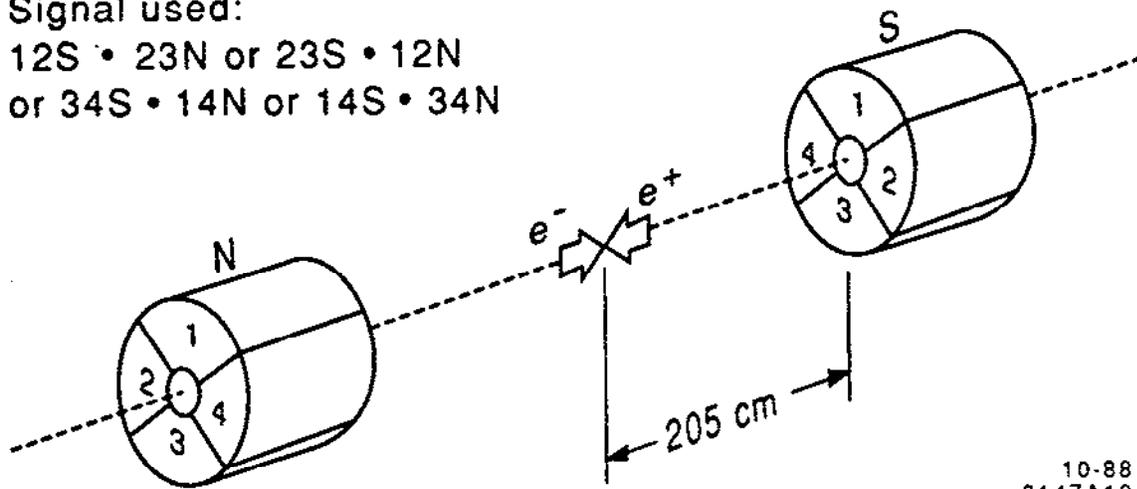
10-88
6147A19

Fig. 23

Fig. 24

Quadrupole
Doublet

Spectrometer
Magnet
Vertical

e^-

Horizontal Bends for
Synchrotron Radiation

Dump

Synchrotron
Light Monitor

4-87

e^+

5771A1

Fig. 25

Fig. 26

Camera

Iris Control

Mirror

Phosphor Screen and
Wire Array

Spectrometer
Beam Deflection

Illumination
Unit

Beam Pipe

Syncrotron Band

3-88
5973A1

Fig. 27

FASTBUS crate segments 27
FASTBUS cable segments 6
SSPs 32

10-88

6147A21

Fig. 28

Vertex Drift Chamber —
(inner Wall)

Silicon Strip —
Detectors

e⁺   e⁻

Beam Pipe

5.2 cm

1 cm

3-87

Fig. 29

Fon-out

38

74-94

Fan-out

14-18

Ceramic

S Detector
(512 Strips)

Thin Cable

Microplex Chips

Capacitors

Hybrid

Support

Soldering

Cable

Fig. 30

GRID

CATHODE

HARP
(guard wires not shown)

MACOR
CERAMIC

ENDPLATE

PRESSURE
HEAD

2-89
6147B33

Fig. 31

Aluminum Outer Shell

HV Skin

Field Shaping Electrode

Cathode - 59 Wires Spaced at 2.0

Field Shaping Wires

Anode Plane - 40
Sense Wires Spaced at 2.9

Grid Planes -
41 Wires Spaced at 2.9

0   50   100
Dimensions in millimeters

3.6

2.9

179.8

15.137°

51.27

Beryllium
Core
HV Skin

45.3

2-85
6147A34

Fig. 32

556 cm

340 cm

y

z

X

IP

Facade

76 cm

122 cm Pb

Fe

198 cm

Shielding

Chambers

12-88

6147A29

Fig. 33

Aluminum Support Structure

Lead Collimators

Connectors for Electronic Readout

Invar

Hexel Aluminum

Wire Array Targets

$D = 27$ cm

Synchrotron Beam

Electron Beam (beam pipe not shown)

10-88
6147A25

Fig. 34